Tropical Intraseasonal Variability Response to Zonally Asymmetric Forcing in an Idealized Moist GCM

Cameron G. MacDonald[a] Yi Ming[b]

[a] *Program in Atmospheric and Oceanic Sciences, Princeton University, Princeton, New Jersey*

[b] *NOAA/Geophysical Fluid Dynamics Laboratory, Princeton, New Jersey*

Corresponding author: Cameron G. MacDonald, cgm3@princeton.edu

ABSTRACT: The tropical intraseasonal variability in an idealized moist general circulation model (GCM) which has a simple moist convection scheme and realistic radiative transfer, but no parameterization of cloud processes is investigated. In a zonally symmetric aquaplanet state, variability is dominated by westward-propagating Rossby waves. Enforcing zonal asymmetry through the application of a prescribed heat flux in the slab ocean bottom boundary leads to the development of a slow, eastward propagating mode which bears some of the characteristics of the observed Madden-Julian Oscillation (MJO). When the ocean heat flux is made stronger, high frequency Kelvin waves exist alongside the MJO mode. The spatial distribution of precipitation anomalies in the disturbances most resemble the MJO when very shallow slab ocean depths (1 m) are used, but the mode still exists at deeper slabs. Sensitivity experiments to the parameters of the convection scheme suggest that the simulated MJO mode couples to convection in a way that is distinct from both Kelvin and Rossby waves generated by the model. Analysis of the column moist static energy (CMSE) budget of the MJO mode suggests that radiative heating plays only a weak role in destabilizing the mode, in contrast to many previous idealized modelling studies of the MJO. Instead, the CMSE budget highlights the importance of the lifecycle of vertical advection for the destabilization and propagation of the MJO. Synergies between the generated MJO mode and linear theories of the MJO are discussed as well.

1. Introduction

The Madden Julian Oscillation (MJO) is the strongest mode of intraseasonal variability observed over the Indo-Pacific warm pool (Madden and Julian 1971, 1972). Unlike other prominent modes of tropical wave variability such as Kelvin waves and Equatorial Rossby waves, the MJO does not appear as a solution to the linear dry equations of Matsuno (1966). The wavenumber-frequency analysis of Wheeler and Kiladis (1999) further confirmed the MJO's existence as a distinct mode from convectively-coupled equatorial Kelvin waves. This has led many to posit that atmospheric water vapor plays a key role in the dynamics of the MJO [See reviews by Zhang et al. (2020) and Jiang et al. (2020) for in-depth discussions of current theories of the MJO]. However, a consistent physical picture of the mechanisms which control the initiation, maintenance and propagation of the MJO has yet to be attained in the fifty years since the identification of the phenomenon.

Moisture mode theories of the MJO (Adames and Maloney 2021) have provided promising insights into the dynamics of the MJO. The concept of a moisture mode, in which the presence of atmospheric water vapor is fundamental to the existence of equatorial wave modes, was defined in a formal manner by Sobel et al. (2001). Subsequent works have looked at how surface heat exhange processes (Neelin et al. 1987; Emanuel 1987) may be responsible for the destabilization of the MJO at planetary scales (Fuchs and Raymond 2005, 2017). Other moisture mode theories (Sobel and Maloney 2012, 2013) have described the dynamical fields of the MJO as being the response to the instantaneous localized heating of the MJO in the spirit of Gill (1980), with the localized heating determined by a prognostic moisture equation. Adames and Kim (2016) further developed this Gill-like response theory for the MJO. Subsequent work has suggested that moisture modes and the MJO may exist on a spectrum of tropical wave species which are differentiated by the interaction of time scales of moist convection, dry gravity waves and the wave itself (Adames et al. 2019).

In moisture mode theories of the MJO, the gross moist stability (GMS) (Raymond et al. 2009; Inoue and Back 2015b) plays an important role. The GMS measures the export of column moist static energy (CMSE) normalized by some measure of the strength of convection. Regions with negative GMS will increase their CMSE, while those with positive GMS will remove CMSE. Some moisture mode theories of the MJO rely on the reduction of the "effective" GMS felt by the column through diabatic effects such as cloud-radiative feedbacks (Adames and Kim 2016; Adames

et al. 2019) to make the GMS negative and thus destabilize moisture modes. Conversely, Fuchs and Raymond (2017) showed that moisture modes may be destabilized at planetary scales in the absence of cloud-radiative effects, with the GMS remaining positive. Inoue and Back (2015b) and Inoue and Back (2017) showed that in reality, the GMS is a highly time-dependent quantity which fluctuates around a characteristic value which is the relevant GMS quantity for linear moisture mode theories. However, this time-dependence has a distinct lifecycle associated with the recharge and discharge of CMSE, with lower GMS occuring before the time of maximum convection, and higher GMS afterwards.

The moisture mode framework is far from the only theoretical explanation that has been posited for the MJO. Recharge-discharge theories of the MJO (Bladé and Hartmann 1993; Hu and Randall 1994) suggest that the observed intraseasonal time scale of the MJO can be attributed to local convective processes associated with the recharge and discharge of column moist static energy. In this view, shallow vertical velocity profiles build up moist static energy within the column, which is then removed by the ensuing deep and then stratiform convection, leading to a period of weakened convection while the column starts to recharge its CMSE. Such theories require an explanation for the preferential development of shallow convection on the eastern margins of the MJO to explain its eastward propagation (Wolding and Maloney 2015). Benedict and Randall (2007) found that frictional moisture convergence in the boundary layer (Wang and Rui 1990; Maloney and Hartmann 1998) could act as a mechanism to initiate this convective lifecycle.

The emergence of further theories in recent years highlights the challenges that still remain in understanding the MJO. Multiscale interaction theories (Majda and Stechmann 2009, 2011) suggest that the MJO is an envelope of smaller-scale convective features which interact non-linearly with tropospheric water vapor. Quasi-equilibrium theories of the MJO hold some similarities to moisture mode theories, and have variants which rely on cloud-radiation interactions to grow at planetary scales (Emanuel 1987) and those that are unstable without such feedbacks (Ahmed 2021). Gravity wave theories of the MJO (Yang and Ingersoll 2013, 2014) posit that the MJO is generated by interference between westward- and eastward-propagating gravity waves when convection is viewed as a triggered process. Still more exotic theories of the MJO have been put forth; the theories of Yano and Tribbia (2017) and Rostami and Zeitlin (2019) suggest that it is non-linearity, rather than tropospheric water vapor which is essential to the presence of an MJO wave mode.

While these theories have elicited varying degrees of attention in the scientific community, none of them is recognized as a complete explanation of the MJO.

In parallel with theoretical developments, idealized modelling studies of the MJO have attempted to elucidate its underlying physical mechanisms. The processes which destabilize and propagate the MJO in zonally symmetric settings have been explored in comprehensive GCMs with traditional convection parameterizations (Carlson and Caballero 2016), super-parameterized convection (Andersen and Kuang 2012; Arnold et al. 2013; Arnold and Randall 2015) and with cloud-resolving resolution (Khairoutdinov and Emanuel 2018). Other studies have instead focused on the role that the Indo-Pacific warm pool plays in the existence of the MJO; Maloney et al. (2010) showed that a stronger MJO could be generated in fixed sea surface temperature (SST) simulations in which the SST distribution mimicked the observed pattern of Earth, relative to zonally symmetric simulations. However, the development of a strong MJO mode in Maloney et al. (2010) also relied on a reduction of the extratropical meridional SST gradient to a quarter of its observed value.

GCMs with simplified convection schemes have seen limited use in studying the MJO. In zonally symmetric configurations, models such as the one described in Frierson et al. (2006, 2007) when augmented with a simplified Betts-Miller convection scheme as in Frierson (2007b) have been shown to produce a robust band of Kelvin waves, but negligible MJO-like variability (Frierson 2007a). When enhanced with full-physics radiative transfer this model was shown to produce monsoon-like seasonal variability without any parameterizations of cloud processes (Clark et al. 2020).

In this study we run the idealized moist GCM of Clark et al. (2020) in an aquaplanet setup with a slab ocean layer below. A zonally asymmetric state is induced via the application of a wavenumber-1 ocean heat flux to generate a warm pool in one hemisphere. This configuration will be shown to favor the generation of an MJO-like equatorial mode which produces slow, eastward propagating signals of precipitation and column water vapor in the warm pool sector. Composite analysis based on the velocity potential difference between the lower- and upper-troposphere suggest that this mode is able to reproduce many of the equatorial and extratropical features of the MJO. The simple convection scheme used in the model allows for a more thorough understanding of how the MJO-like mode couples to moist convection.

The remainder of this paper is structured as follows: Section 2 describes the idealized moist GCM, experimental setups and analysis techniques used in the study. Section 3 describes the characteristics of the mean state and tropical variability of these simulations. Section 4 discusses the sensitivity of the tropical waves generated in the model to a few key parameters. Section 5 analyzes the column moist static energy budget of the MJO-like disturbances in the model, and discusses its connection to linear theories of the MJO. This is followed by a discussion and a summary of results in Sections 6 and 7, respectively.

2. Methods

a. Model Description

An idealized moist GCM is used to perform numerical experiments in this study. The modeling setup is built upon the idealized moist model of Frierson et al. (2006, 2007), with some modifications of parameterized physical processes as in Frierson (2007b) and Clark et al. (2018). The model has a spectral dynamical core that is run at T42 resolution, corresponding to 128 grid points in longitude and 64 grid points in latitude. The vertical structure of the model is that of Clark et al. (2020), with 40 unevenly-spaced vertical levels. The bottom boundary of the model is a mixed layer slab ocean with a uniform depth. The thermodynamic budget of this slab layer is

$$\rho_O c_{pO} d \frac{\partial T_s}{\partial t} = S - L - L_v E - H - \nabla \cdot \mathbf{F_O}, \tag{1}$$

where ρ_O is the density of the layer, c_{pO} its specific heat capacity, d the depth of the mixed layer and T_s its temperature. Forcing terms are on the right hand side, where S represents incoming shortwave radiation, L outgoing longwave radiation at the surface, $L_v E$ latent heat fluxes and H sensible heat fluxes. The final term on the right hand side is the convergence of ocean heat fluxes. In this study, the ocean heat flux convergence will be prescribed to generate zonal asymmetry in the model.

In our model, the condensation of water vapor in the atmosphere releases latent heat, so that the hydrological cycle may influence the general circulation of the atmosphere (Frierson et al. 2006). Moist convection is parameterized as in Frierson (2007b) using a simplified Betts-Miller convection scheme (Betts and Miller 1986; Frierson 2007b). In this scheme temperature is relaxed

back to a moist adiabat and water vapor is relaxed to a constant relative humidity that consumes any positive convective available potential energy (CAPE) in the atmospheric column (Frierson 2007a). This formulation introduces two parameters into the model: a moist convective adjustment time τ_{SBM} which controls how quickly temperature and moisture are returned to their reference profiles, and the relative humidity $\mathrm{RH}_{\mathrm{SBM}}$ which the moisture profile is relaxed back to. Previous studies have suggested that both the zonally averaged circulation (Frierson 2007b) and equatorial wave variability (Frierson 2007a) are sensitive to the values of these convection scheme parameters. Precipitation is instantly rained out when the criterion for convection or large scale condensation (saturation at the grid scale) is satisfied, such that this model does not contain any clouds.

The changes introduced to the model in Clark et al. (2018) amount to adding a full-physics radiative transfer module to the model (Paynter and Ramaswamy 2014) to replace the gray-radiation scheme of Frierson et al. (2006, 2007), and using the planetary boundary layer scheme of O'Gorman and Schneider (2008). The use of the full-physics radiation allows for feedbacks between water vapor and radiation (Clark et al. 2018). The alternative boundary layer formulation is allowed to be unstable, in contrast to the original parameterization of Frierson et al. (2006, 2007) which could only be stable or neutral. This original scheme has been shown to support a robust spectrum of convectively-coupled equatorial Kelvin waves (Frierson 2007a); we will show that a broader selection of equatorial waves can be simulated when the boundary layer is allowed to become unstable. The set of physical parameterizations as decribed is similar to those used in Merlis et al. (2013).

b. Model Experiments

1) Core Model Experiments

Our control experiment consists of a zonally symmetric aquaplanet with a mixed layer depth of 1 m. The moist convective adjustment time is set to 2 h, following the suggestion of Betts and Miller (1986) and consistent with previous studies using similar modelling setups (Frierson 2007b,a; O'Gorman and Schneider 2008; Clark et al. 2018, 2020), and the relative humidity of the reference moisture profile is set to 70%. We run this experiment for 20 years in a perpetual equinox state, so that the sub-solar point always lies on the equator and there is no seasonal cycle. Analysis is performed on years 10 through 20 of the simulation. In this control setup with a shallow mixed

layer, the model likely equilibrates much faster than the 9 years that are discarded (Clark et al. 2018), however we retain this spin-up discard to be consistent with further sensitivity experiments that are run with a deeper mixed layer.

To perturb the control experiment from its zonally symmetric state, we introduce a zonally asymmetric ocean heat flux divergence in the mixed layer ocean. The ocean heat flux pattern is sinusoidal in longitude with a wavenumber-1 pattern, and equatorially trapped with a gaussian meridional profile using a RMS width of 18° in latitude. This selected pattern correspondingly generates a wavenumber-1 pattern in the surface temperature of the mixed layer ocean to mimic, in an idealized sense, the Indo-Pacific warm pool present on Earth. In our case the cold-pool region resides in the eastern hemisphere (0°E - 180°E) and the warm pool in the western hemisphere (180°E - 360°E). In using a sinusoidal pattern for the ocean heat flux divergence, no additional energy is added into the system through the bottom boundary in the global average. We run three different zonally asymmetric experiments with the amplitude of the ocean heat flux set to 25 W m^{-2}, 50 W m^{-2} and 100 W m^{-2}. These three amplitudes correspond to equatorial temperature contrasts of about 2 K, 5 K and 10 K respectively. Throughout the rest of the paper, these three experiments will be referred to as Q25, Q50 and Q100.

2) Sensitivity Experiments

In addition to the core experiments described above, we run a number of additional experiments to explore the sensitivity of the model state (in particular the sensitivity of its equatorial wave variability) to some key parameters in the model in the asymmetric state. Firstly, we run experiments with different depths of the ocean mixed layer. Using the Q50 case as a starting point, we perform model runs with the mixed layer depth of the ocean set to 20 m and 100 m.

We also run experiments similar to Frierson (2007a) to test the sensitivity of the model to the parameters of the convection scheme. Again using the Q50 run as the base point about which we perturb the model, we perform two additional experiments where the relative humidity of the reference moisture profile (RH_{SBM}) is varied: one where we decrease RH_{SBM} to 60% and another where it is increased to 80% compared to its control value of 70%. One additional test of the sensitivity to the convection scheme is performed by increasing the moist convective adjustment time τ_{SBM} to 16 h from its initial value of 2 h. This brings τ_{SBM} onto the same order as calculated

in observational studies of tropical precipitation (Adames 2017), as well as being the point at which Frierson (2007b) observed a transition in the strength of the zonally averaged circulation in a zonally symmetric configuration.

c. Analysis Techniques

1) Space-time Spectral Analysis

The main interest of this study is the tropical wave variability of the equatorial belt. To further elucidate the behavior of these waves, we transform various fields into their space-time spectral representations to isolate modes at specific wavenumbers and frequencies. We employ the Fast-Fourier Transform (FFT) method of Welch (1967) as described by Wheeler and Kiladis (1999). The time series of a variable is split into a series of 192-day segments which overlap by 96 days, and a Hanning window is applied to taper the ends of the segments. The FFT is then applied to the time and longitude directions, and the resulting spectral representation is averaged over each segment and each latitude from 10°S to 10°N weighted by the surface area of the grid cells at each latitude. A red spectrum is computed by applying a 1-2-1 filter 40 times along the frequency dimension and 10 times along the wavenumber dimension. Finally we calculate the signal strength S at each wavenumber and frequency as in Clark et al. (2020) by

$$S = \frac{P - R}{P}, \tag{2}$$

where P is the power spectrum and R is the red spectrum.

To determine the statistical significance of the signal strength, we employ a chi-squared test at the 99% level. Wheeler and Kiladis (1999) calculate the number of degrees of freedom for the normalized power P/R as

$$n = \frac{2\ \text{(amplitude and phase)} \times 11\ \text{(years)} \times 8\ \text{(latitudes)} \times 365}{192\ \text{(segment length)}} \approx 335, \tag{3}$$

so that the critical value of the normalized power is $(P/R)_c = \chi_c^2/(n-1) = 1.19$, where χ_c^2 is the value of the chi-squared cumulative distribution function at its 99th percentile. Transforming this critical normalized power into a critical signal strength as in Clark et al. (2020), we find that the criterion for significance is $S > 0.16$.

2) Lagged Regression Analysis

Lagged regression analysis is used to construct composite tropical disturbances out of the model time series. Indices for the regressions are calculated by spectrally filtering equatorial precipitation anomalies to retain only the variability associated with the spectral region of the waves of interest. This index is then standardized by removing its time mean and normalizing by its standard deviation, providing a non-dimensional vector $\hat{\mathbf{P}}$ which we can regress against any variables output from the model (Adames and Wallace 2014a; Adames and Kim 2016; Clark et al. 2020). Specifically, regression maps are calculated as

$$\mathbf{D} = \frac{\mathbf{S}\hat{\mathbf{P}}^{\mathrm{T}}}{N}, \tag{4}$$

where the rows of the matrix $\mathbf{S}$ contain the time series of the regressed variable at each grid cell (and vertical level for three-dimensional fields), and N is the number of entries in the time series. By shifting the index in time, we can calculate regression maps lagging or leading the index and view the time evolution of the composite event.

The statistical significance of the regression coefficients contained in $\mathbf{D}$ are evaluated using a two-tailed Student's t-test at the 99% significance level, with the number of degrees of freedom equal to the number of entries in the time series. From this test, regression values are considered significant if the correlation coefficient of the regression is greater than 0.02. Multiplying by the standard deviation of the time series in question then gives a critical magnitude for the regression coefficient above which results are considered statistically significant.

3) Velocity Potential Indices for Intraseasonal Oscillations

To further evaluate the three-dimensional structure of eastward-propagating planetary-scale waves with intraseasonal time scales, we also utilize the principle component analysis (PCA) techniques described in Adames and Wallace (2014a). The PCA is performed on the velocity potential difference ($\Delta\chi$) between the 850 hPa and 150 hPa isobaric levels. As described in Adames and Wallace (2014a), since the velocity potential is the inverse Laplacian of the divergence field, it captures primarily convergence which occurs on the planetary scale. Upper-level divergence (convergence) and lower-level convergence (divergence) will then be associated with positive (negative) values of $\Delta\chi$.Adames and Wallace (2014a) show that this velocity potential index performs simi-

larly to other MJO indices such as the real-time multivariate (RMM) MJO index of Wheeler and Hendon (2004). The RMM index uses outgoing longwave radiation (OLR) as one of its predictors; in our cloud-free model OLR may have different characteristics to that of Earth, and so we prefer the velocity potential index which relies only on dynamical fields. In atmospheres which support intraseasonal oscillations, such as the MJO on Earth, the resulting first two empirical orthogonal functions (EOFs) yield wavenumber-1 patterns that are in quadrature with one another. An index for any phase α of the MJO can then be constructed using the principal components of the EOF1 and EOF2:

$$\hat{P}(t) = \mathrm{PC}_1(t)\cos\alpha + \mathrm{PC}_2(t)\sin\alpha, \tag{5}$$

where PC_1 and PC_2 are the PCs corresponding to the EOF1 and EOF2, respectively. Regressions of the form of Eq. 4 can then be carried out using these indices. Under this convection and using the same sign conventions for EOF1 and EOF2 as Adames and Wallace (2014a), $\alpha = 0^\circ$ and $\alpha = -90^\circ$ would correspond to an active MJO over the Maritime Continent and the Indian Ocean, respectively. In our asymmetric experiments, these phases correspond to an active MJO over the center of the warm pool (270°E) and the western region of the warm pool (180°E), respectively. In the context of the RMM index of Wheeler and Hendon (2004), these two values of α correspond roughly to Phase 4 and Phase 2, respectively (Adames 2017).

To construct summaries of a composite ISO over its active phase, we use the "warm-pool compositing" technique described in Adames and Wallace (2014b, 2015). Regression maps at equally spaced intervals (1/32 of the MJO phase) are averaged after shifting the maps in longitude so that either (a) its maximum in $\Delta\chi$ or (b) its minimum in $\partial\Delta\chi/\partial x$ are located at the same reference longitude. As in Adames (2017), these two summary maps will be referred to as (a) warm pool composite 1 (WPC1) and (b) warm pool composite 2 (WPC2), respectively. We could formally write these composites as

$$\mathrm{WPC1}(\mathbf{D}) = \frac{1}{\pi}\int_{-\pi/2}^{\pi/2} \mathbf{D}(\alpha, \lambda + \lambda_{r1}(\alpha), \varphi, p)\mathrm{d}\alpha \quad \text{and} \tag{6a}$$

$$\mathrm{WPC2}(\mathbf{D}) = \frac{1}{\pi}\int_{-\pi/2}^{\pi/2} \mathbf{D}(\alpha, \lambda + \lambda_{r2}(\alpha), \varphi, p)\mathrm{d}\alpha, \tag{6b}$$

where $\lambda_{r1}(\alpha)$ is the longitude at which $\Delta\chi$ reaches it maximum and $\lambda_{r2}(\alpha)$ is the longitude at which $\partial\Delta\chi/\partial x$ reaches its minimum. Significance criteria for the warm pool composites are treated in a similar manner to the lagged regression analysis.

3. Results

a. Mean State Response to Asymmetric Forcing

To begin our presentation of the simulation results, we look at how the addition of the zonally asymmetric ocean heat flux influences the time-mean and zonal-mean state of the climate. Fig. 1a shows the meridional distribution of the zonally-averaged surface temperature for the control run and the Q25, Q50 and Q100 experiments. The temperature distribution in the mid-latitudes remain quite similar between experiments. At the equator, the meridional gradient of the surface temperature is reduced as the amplitude of the forcing is increased, such that the bump that is observed at the equator in the control run has been completely smoothed out in the Q100 run. Frierson (2007b) observed a similar bump appear when changes were made to the convection scheme of their zonally symmetric model.

Fig. 1b shows the zonal distribution of surface temperatures at the equator. It should be noted that since the model is run on a Gaussian grid, "equatorial" values are actually the average of the two grid cells whose boundary lies on the equator. The inclusion of the ocean heat flux cools the surface temperatures of the eastern hemisphere and warms those of the western hemisphere. Since the zonal-mean surface temperature decreases as the forcing is increased, we see that the cold hemispheres are colder relative to the control run than the warm hemispheres are warm.

The vertically and zonally integrated meridional moist static energy (MSE) transport is shown in Fig. 1c, where the transport has been decomposed into contributions from its mean component, $[\overline{v}][\overline{h}]$, its stationary eddy component $[\overline{v}^*\overline{h}^*]$ and its transient component $\overline{[v'h']}$, where v is the meridional wind and h is the MSE. Here overbars represent time means, square brackets represent zonal means, primes indicate deviations from the time mean and stars indicate deviations from the zonal mean. The energy transport is dominated by the contribution from transient eddies, especially in the mid-latitudes. The relative importance of the contributions from each of mean, stationary eddy and transient parts of the energy transport remains largely the same across all the runs; in the Q100 case the mid-latitudes show a weakening of the transient from transient motions,

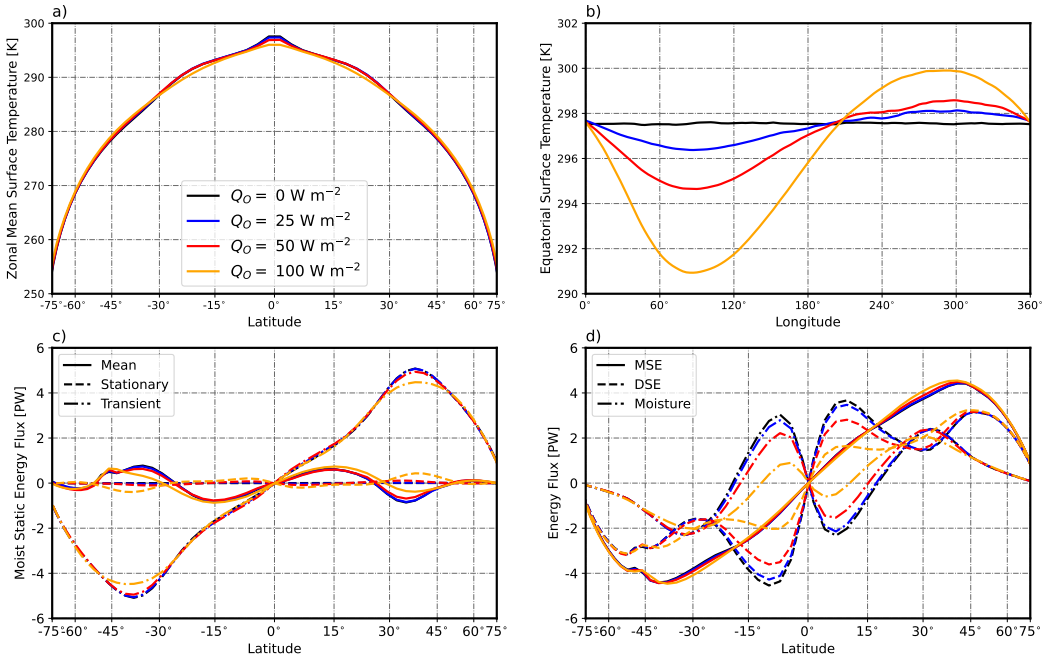

FIG. 1. (a) Meridional distribution of the zonally-averaged surface temperature for the control run and the Q25, Q50, and Q100 experiments. The meridional axis scales with the sine of latitude to accentuate the tropical belt. (b) Zonal distribution of surface temperatures at the equator for the control run and the three zonally asymmetric experiments. (c) Decomposition of vertically and meridionally integrated meridional energy flux into its mean (solid lines), stationary eddy (dashed lines), and transient eddy (dash-dotted lines) components for each experiment. (d) Total meridional energy flux (solid lines) and its decomposition into its contributions from dry static energy (dashed lines) and moisture (dash-dotted lines) for each experiment.

but this is compensated by an increase in the MSE transport by stationary eddies. In the tropics the decomposition of the MSE transport looks almost identical across all the runs.

While the picture of the meridional MSE transport remains consistent as the strength of the asymmetric forcing is increased, its individual contributions from the transport of dry static energy (DSE) and moisture change significantly in the tropics. Fig. 1d shows the total meridional energy transport and its decomposition into transport of DSE and moisture. While the total MSE transport (solid lines) remains largely the same with varied asymmetric forcing, the magnitudes of the DSE transport (dashed lines) and moisture transport (dash-dotted lines) reduce as the strength of the asymmetric forcing is increased in such a way that their sum remains virtually unchanged. The contributions of DSE and moisture in the extratropics are qualitatively unaffected by the addition of

the asymmetric forcing until the Q100 case, when DSE (moisture) transport increases (decreases) slightly.

The inclusion of the zonally asymmetric ocean heat flux has profound effects on the zonal mean circulation of the atmosphere. Fig. 2 shows the meridional overturning circulation and zonal-mean zonal winds for each run. In the control run (Fig. 2a), we observe the familiar equinoctial Hadley cell (HC) structure and westerly sub-tropical jets (STJs) in the mid-latitudes of each hemisphere. As the forcing is increased, the tropical upper troposphere develops westerly winds and begins to superrotate: in the Q25 run (Fig. 2b), this superrotation is weak, and the zonal-mean zonal winds are similar to the control run. When the strength of the forcing is doubled in the Q50 run (Fig. 2c) the superrotation has strengthened so that the upper tropospheric zonal winds are on the order of 10 m s^{-1}, and the strength of the STJs has weakened considerably. After a further doubling (Fig. 2d), an equatorial westerly jet forms at the equator and the STJs have moved slightly equatorward. The zonal distribution of upper tropospheric winds (not shown) reveal that the superrotation is driven by strong westerly winds in the cold hemisphere, where the STJs have been eliminated such that the upper tropospheric dynamical fields form a coupled Kelvin-Rossby (KR) pattern (Showman and Polvani 2011). The development of superrotation as a result of asymmetric forcing is consistent with previous studies using both two-layer models (Suarez and Duffy 1992; Saravanan 1993) and dry multi-level GCMs (Kraucunas and Hartmann 2005; Lutsko 2018).

The strength of the HC is also affected by the asymmetric forcing. The overturning streamfunction for the Q100 case shown in Fig. 2d is about half the strength of the control run (Fig. 2a). This transition to a weaker HC occurs rather abruptly between the Q50 and Q100 runs, whereas the transition to equatorial superrotation occurs smoothly as the asymmetric forcing is increased. Kraucunas and Hartmann (2005) also saw a reduction in the strength of the HC after imposing a zonal wavenumber-2 heating distribution in their dry multi-level GCM. That the strength of the HC decreases in tandem with the transport of DSE while the MSE transport remains the same (Fig. 1d) suggests that the dry thermodynamics plays a role in setting the strength of the HC in these experiments.

To finish the discussion of the model mean state response to asymmetric forcing, Fig. 3 shows the distributions of time mean precipitation and column saturation fraction (Bretherton et al. 2004; Adames 2017), which is defined as $\langle\overline{q}\rangle/\langle\overline{q_s}\rangle$, where q is the specific humidity, q_s the saturation

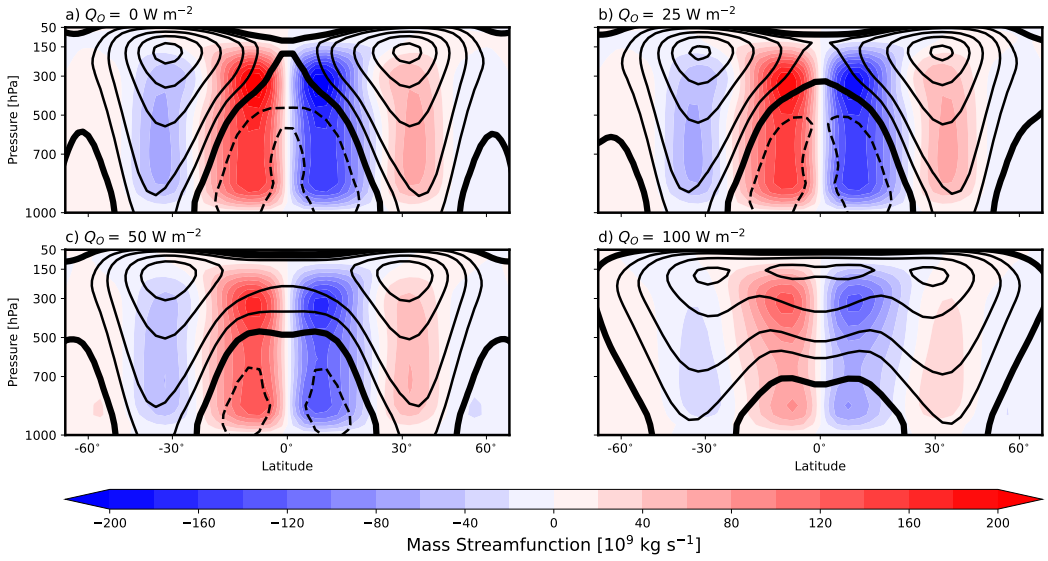

FIG. 2. Eulerian mass streamfunction (shading) and zonal mean zonal wind (black contours) for (a) the control run, (b) the Q25 run, (c) the Q50 run and (d) the Q100 run. The thick black contour shows the zero line of zonal mean zonal wind, and the contour interval is 10 m s^{-1}, with additional contours added at the -5 and +5 m s° levels.

specfic humidity, the overbar indicates a time mean, and the angle brackets indicate a pressure integral from the surface to 100 hPa. In the control, Q25, and Q50 experiments (Fig. 3a-c), precipitation can be well-described as a function of the column saturation fraction; the drying of the tropics in the cold hemisphere and the subtropics in the warm hemisphere are captured in both fields. Furthermore, in these three experiments the climatologically wet regions ($\overline{P} > 100$ W m^{-2} ≈ 3.6 mm day^{-1}) are enclosed in the regions of the tropics where the column saturation fraction exceeds the relative humidity of the reference moisture profile of the model's convection scheme $\mathrm{RH}_{\mathrm{SBM}}$ (the thick red contour in Fig. 3). In all three cases this wet regions extends across the entire tropical belt.

The Q100 case (Fig. 3d) contains much more significant departures from the control run. The cold hemisphere now contains a large dry region in the tropics with mean precipitation less than 50 W m^{-2}, while the subtropics of this hemisphere have become much wetter. Along with the strong mean precipitation of the tropics in the warm hemisphere, this lends a wavenumber-1 KR pattern to the mean precipitation. There is also less coherence between the precipitation and column

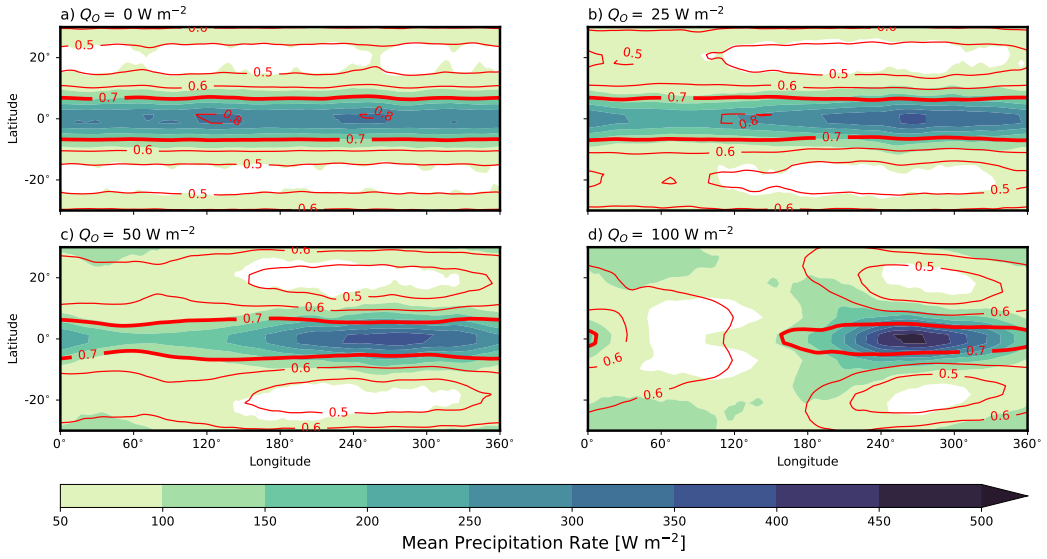

FIG. 3. Time-mean precipitation (shading) and column saturation fraction (red contours) for (a) the control run, (b) the Q25 run, (c) the Q50 run and (d) the Q100 run. The thick contour shows the Simplified Betts-Miller relative humidity used in the convection scheme

saturation fraction; in the western portion of the warm pool there are wet regions which reside outside the region in which $\langle\overline{q}\rangle/\langle\overline{q_s}\rangle > \mathrm{RH_{SBM}}$.

The response of the model to asymmetric forcing is characterized by a smooth transition to a superrotating state and an increase (decrease) in tropical precipitation in the warm (cold) hemisphere. After the strength of the forcing is increased enough to generate climatologically dry regions in the tropics, more abrupt transitions to a weaker HC and wetter subtropics in the cold hemisphere are observed.

b. Tropical Variability Response

We next investigate the response of tropical wave activity to asymmetric forcing. Fig. 4 shows Hövmoller plots of equatorial precipitation averaged over 10°S to 10°N for 200 day segments each experiment. For the control run shown in Fig. 4a, the dominant mode of variability is westward propagating Rossby waves, which exist throughout the entirety of the domain. Upon the addition of the asymmetric forcing in the Q25 case (Fig. 4b), a new mode of intraseasonal tropical variability emerges alongside the Rossby waves. These waves propagate eastward with a phase speed of

around 6 m s^{-1} (shown by the red dash-dotted lines in Fig. 4) and are most active over the warm pool sector. These are both fundamental characteristics of the observed MJO on Earth.

Upon a further increase in the strength of the asymmetric forcing in the Q50 case (Fig. 4c), these eastward-propagating waves clearly become the dominant mode of tropical variability. Whereas in the Q25 case these intraseasonal oscillations seemed to be isolated events, in the Q50 case we see multiple MJO-like events occurring successively between days 80 and 160 of the time series. The Q50 case also exhibits states of convective self-aggregation; for the first 80 days of the time series, a stationary region of precipitation exists on the western edge of the warm pool around 180°E before it eventually appears to trigger an MJO-like event around day 80.

Fig. 4d shows a Hövmoller plot for the Q100 case. Here we see another transition on the behavior of tropical waves. The first 80 days of the time series are dominated by high frequency Kelvin wave activity over the warm pool sector, while days 80-160 contain a series of strong, successive MJO events before returning to a Kelvin wave dominated regime for the final 40 days. Interestingly, these two regimes appear to be mutually exclusive: the Kelvin wave activity vanishes from the tropical belt when the MJO is active and vice versa. This is in contrast to observational analysis such as that of Wheeler and Kiladis (1999), which suggests that an active MJO may coexist with Kelvin waves (cf. their Fig. 9). In this strongest forcing case, virtually all precipitation variability has been eliminated from the cold pool sector.

We next transform these equatorial precipitation time series into their signal strength in spectral space using the method described in Section 2c1. Since we choose to segment the times series into into 192-day periods, the Hövmoller plots in Fig. 4 are representative of what each segment would look like. Fig. 5a shows the signal strength of precipitation for the control run. Consistent with the Hövmoller plot, the strongest signal comes from Rossby waves at zonal wavenumber $k = -5$. There is some spurious eastward propagating signal at intraseasonal time scales and in the Kelvin wave band. For the Q25 case (Fig. 5b) a stronger MJO signal is observed between $k = 2$ and $k = 5$. This signal falls approximately along the 6 m s^{-1} phase speed line (the thick blue dashed line in Fig. 5). Moving on the Q50 case in Fig. 5c, the MJO spectral region overtakes the Rossby waves as the mode with the strongest signal. In the Q100 case (Fig. 5d), high frequency Kelvin wave activity now appears as a large source of variability, while essentially all of the westward-propagating disturbances have been eliminated. Most of the Kelvin wave variability lies between

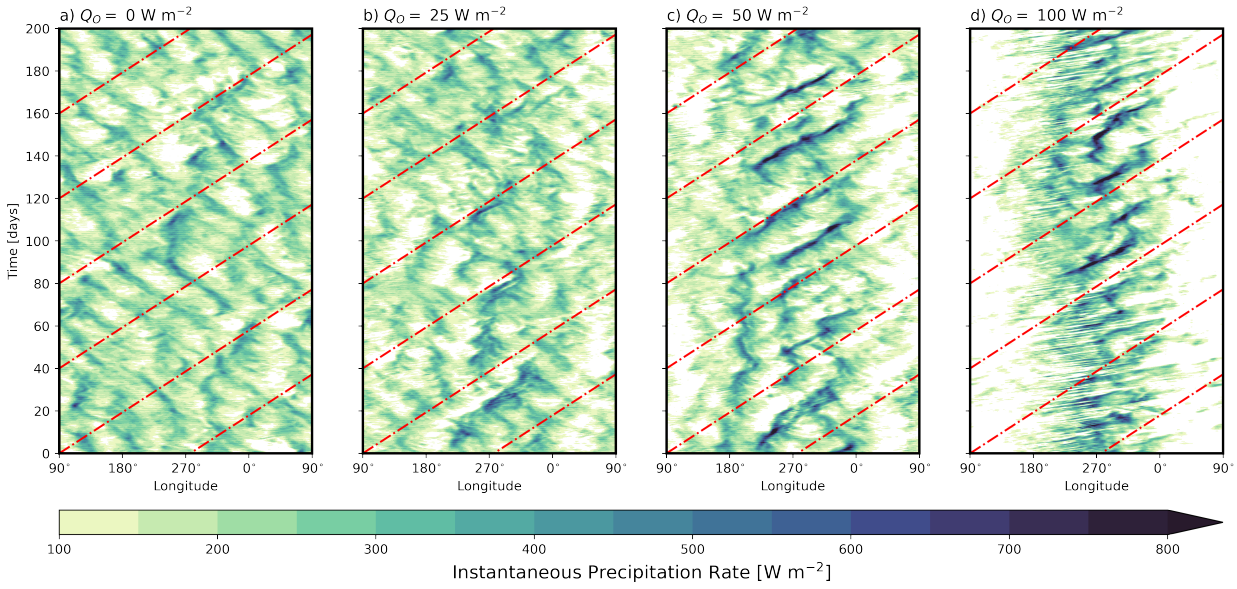

401 FIG. 4. Hövmoller plots of precipitation for (a) the control run, (b) the Q25 run, (c) the Q50 run and (d) the
402 Q100 run, with shading showing instantaneous precipitation averaged from 10°S - 10°N for 200 day segments
403 of the model runs. Red dash-dotted lines show lines of 6 m s^{-1} eastward phase speed, which is about the speed
404 the simulated MJO disturbances travel across the warm pool. The images have been shifted in longitude so that
405 the warm pool lies at the center of the frame.

418 the 50 m and 150 m equivalent depth dispersion curves, so these waves travel faster than observed
419 convectively coupled Kelvin waves on Earth, which have an equivalent depth of 25 m (Wheeler
420 and Kiladis 1999). Frierson (2007a) also found that Kelvin waves propagated faster than observed
421 in the gray-radiation equivalent of this model. Once again the strongest signal appears along the
422 6 m s^{-1} phase speed line, indicating that the MJO mode is a robust feature of all the asymmetric
423 experiments.

429 To view the time evolution of the MJO mode generated by the model, we use lag regression
430 analysis as described in Section 2c2. As an index we use equatorial precipitation filtered to include
431 variability only on intraseasonal timescales (10-100 days) and eastward planetary scales (zonal
432 wavenumbers 1-10) and averaged over the region 265°E-275° and 10°S-10°N. The lower bound of
433 the intraseasonal frequency range has been decreased to 10 days from the more common bound of
434 20 days as this was found to better capture precipitation anomalies in Hövmoller plots (not shown).
435 Precipitation and mid-tropospheric RH are then regressed against this index for lags ranging from -

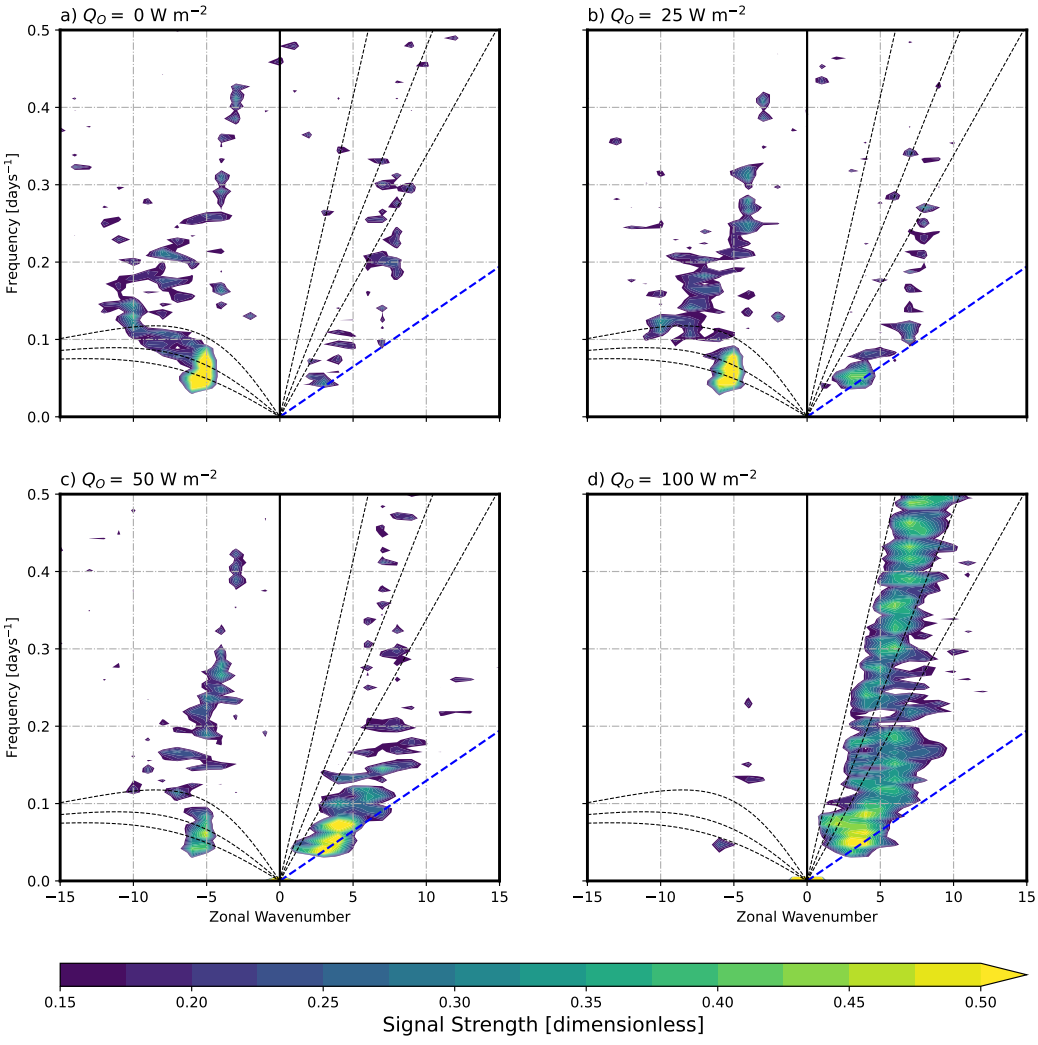

424 FIG. 5. Space-time power spectra of equatorial precipitation (a) the control run, (b) the Q25 run, (c) the Q50
425 run and (d) the Q100 run. Shading shows the normalized signal strength of precipitation averaged from 10°S to
426 10°N. Dashed black lines show dispersion curves for Kelvin and n = 1 Equatorial Rossby waves with equivalent
427 depths of 25, 50 and 150 m. The thick blue dashed line shows the 6 m s^{-1} phase speed line. Only values which
428 pass a chi-squared significance test are shaded.

436 30 days to +30 days. The resulting lagged time series for the control run and the zonally asymmetric
437 experiments are shown in Fig. 6. The strength of the composite MJO increases considerably from
438 the control run to the Q25 run. In all cases, RH anomalies propagate in unison with precipitation,
439 highlighting the strong connection between moisture anomalies and precipitation driven by the
440 model's convection scheme.

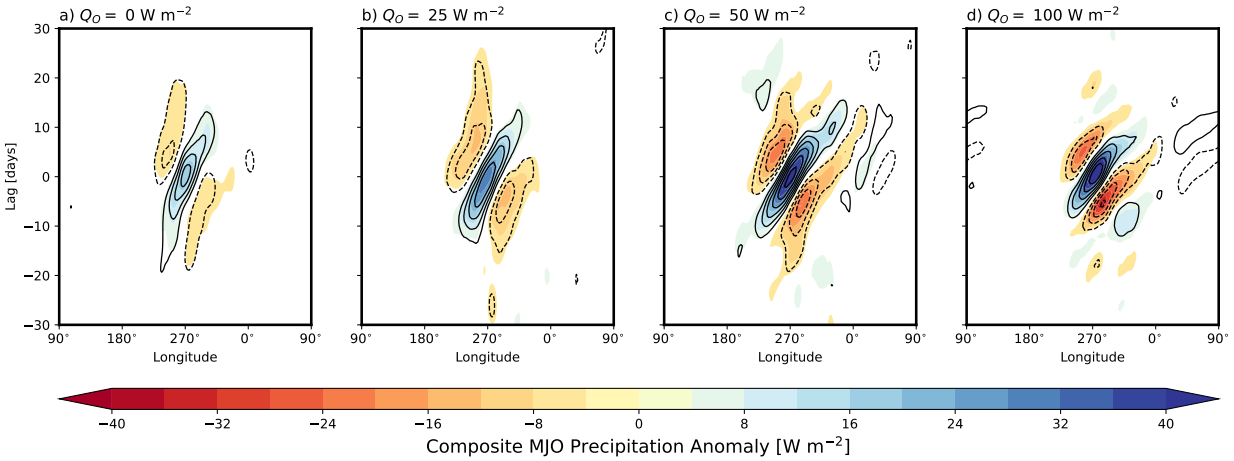

FIG. 6. Lagged time series of a composite MJO for (a) the control run, (b) the Q25 run, (c) the Q50 run and (d) the Q100 run. Shading shows precipitation averaged between 10°S and 10°N, and contours show RH at 400 hPa. The contour interval is 2%, with negative contours dashed and the zero contour omitted. Values which do not pass a two-sided t-test for significance are masked in white. Images have been shifted such that the warm pool lies at the center of the frame.

A robust feature across all the lagged time series in Fig. 6 is the apparent westward group velocity of the simulated MJO. This can be seen by tracking the location of the consecutive peaks and troughs in precipitation: the dry phase which follows the convectively active phase of the MJO occurs significantly further west than the preceding dry phase. Adames and Kim (2016) observed a similar westward group velocity in regressions of reanalysis data onto a MJO-filtered index of outgoing longwave radiation (OLR). Chen and Wang (2018) argued that the westward group velocity reported in Adames and Kim (2016) was a result of the spectral filtering used in that study, which filtered out sub-planetary scale effects related to the transit of the MJO across the Maritime Continent (MC). However, our aquaplanet model produces an apparent westward movement of precipitation maxima without the presence of the MC.

c. Three-dimensional Structure of the Simulated MJO

We now employ the EOF-based regressions described in Section 2c3 to investigate the three-dimensional structures of the intraseasonal disturbances that are prominent in the warm pool sectors of the three asymmetric simulations. Fig. 7a shows WPC1 of precipitation and mid-tropospheric pressure velocity for the Q25 run. This case exhibits characteristics associated with the MJO in

previous studies of reanalysis products (Adames and Wallace 2014b, 2015; Adames 2017). Most notable is the swallow-tail shape of the the main precipitation anomaly, with an equatorially trapped signal leading the reference longitude and two off-equator anomalies at around 10°N/S lagging the reference longitude. The pressure velocity has a similar swallow-tail shape. These figures also highlight the extratropical interactions of the simulated MJO: regions of anomalously high precipitation and ascent are located at 30°N/S around 60° ahead of the convective center of the disturbance, and regions anomalously low precipitation and subsidence about 150° ahead of the disturbance.

Fig. 7b shows the same composited fields for the Q50 case. The zonal extent of the main precipitation disturbance has decreased, but the striking resemblance to the observed MJO is retained; disparities with the equivalent reanalysis-based composites in Adames (2017) can in part be attributed to the northward displacement of the inter-tropical convergence zone (ITCZ) on Earth over the Eastern Pacific, whereas in our model the ITCZ lies on the equator across the entire tropical belt. Additionally, the extratropical regions of ascent and descent are considerably stronger than in the Q25 run. WPC1 for the Q100 run is shown in Fig. 7c. Here some of the resemblance to the observed MJO has been lost, as the precipitation field exhibits less of a swallow-tail shape than in the previous two runs, and the disturbance has become more closely trapped to the equator. The extratropical features however retain their previous structure, and are of a similar strength to those observed in the Q50 case.

Just as the observed MJO is not simply an equatorially-trapped phenomenon, but is rather a circulation with global impacts, the extratropical features shown in Fig. 7 indicate that the simulated MJO mode in our model also has wider interactions. To further investigate this idea, Fig. 8 shows WPC1 and WPC2 the meridional distributions of zonal wind and geopotential height averaged between 20°W and 20°E of their respective reference longitudes. The composites for the Q25 case are shown in Fig. 8a-b. The WPC1 cross-section, which captures behavior over the convective center of the MJO, shows easterly winds at the equator and westerly winds in the extratropics trapped equatorward of the STJs, while the geopotential field exhibits two positive gyres in the upper-troposphere of the extratropics and negative anomalies in the mid-latitudes. The vertical structure of these extratropical geopotential anomalies is thus highly baroclinic, with reversed sign between the lower- and upper-troposphere. WPC2, which leads the convective center,

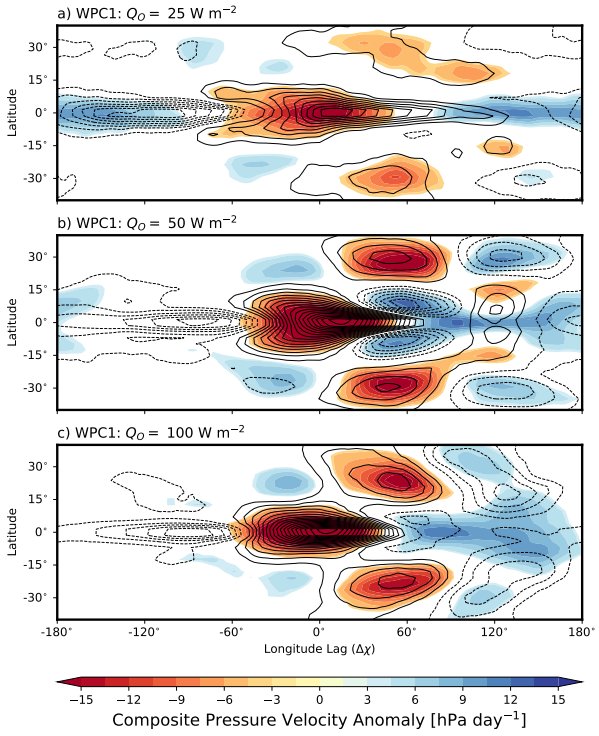

480 FIG. 7. WPC1 of precipitation (contours) and 400 hPa pressure velocity (shading) anomalies for (a) the Q25
481 run, (b) the Q50 run and (c) the Q100 run. The contour interval for precipitation is 3 W m^{-2}, with negative
482 values dashed and the zero contour omitted. Values which do not pass the statistical significance test are masked
483 with white.

495 has a clear equatorially trapped Kelvin wave signal in the upper troposphere, with westerly winds
496 and positive geopotential anomalies. The extratropics are dominated by negative geopotential
497 anomalies with more baroptropic structures than those seen in WPC1. A similar structure to the
498 zonal wind and geopotential fields was observed by Adames and Wallace (2014a) in their study of
499 the MJO using reanalysis data (cf. their Fig. 3).

500 Fig. 8c-d shows similar composites for the Q50 case. These bear a strong resemblance to those
501 of the Q25 case, but with generally stronger anomalies. In particular, the baroptropic extratropical
502 geopotential anomalies are more apparent in WPC2. These anomalies are reminiscent of the
503 "Flanking Rossby waves" identified by Adames and Wallace (2014a) as the primary extratropical
504 features of the observed MJO. When the strength of the asymmetric forcing is increased further
505 in the Q100 case (Fig. 8e-f), the response of the zonal wind and geopotential fields changes
506 significantly, resulting in patterns which bear less resemblance to the observed MJO. In WPC1 the

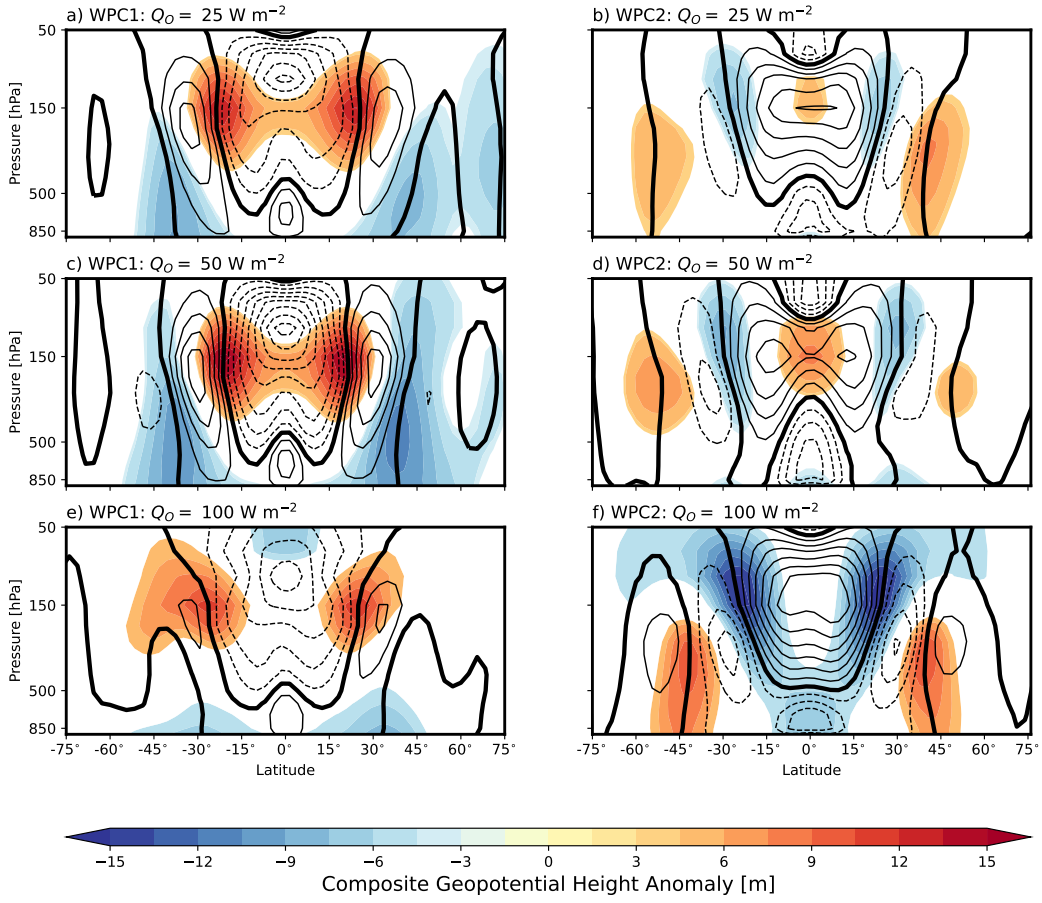

514 FIG. 8. Warm pool composites of geopotential height (shading) and zonal wind anomalies (black contours)
515 averaged between 20°W - 20°E of the reference longitude for (a)-(b) the Q25 run, (c)-(d) the Q50 run and (e)-(f)
516 the Q100 run. Contour interval for zonal wind is 0.5 m s^{-1}, with the thick line indicating the zero contour. Values
517 which do not pass the statistical significance test are masked with white.

507 positive geopotential anomalies have shifted poleward, and there is a stronger negative anomaly
508 present in the lower stratosphere. In WPC2, the equatorial Kelvin wave signal is now dominated by
509 the Flanking Rossby waves, which are now much stronger than in the Q25 and Q50 cases. These
510 results suggest that beyond simply producing a robust intraseasonal oscillation, the Q25 and Q50
511 configurations of our model produce global circulations with properties similar to the MJO, while
512 the Q100 case produces an intraseasonal oscillation with global interactions that are more disparate
513 from the observed MJO.

518 To conclude this section, we look at the anomalous moisture and overturning circulation of
519 simulated MJO events in the equatorial plane. Fig. 9 shows MJO-related anomalies of RH,

specific humidity and zonal circulation. For the Q25 case (Fig. 9a), WPC1 gives a roughly zonal wavenumber-1 pattern in the moisture fields. Specific humidity anomalies are confined below around 300 hPa, while relative humidity anomalies extend through the upper-troposphere to above 100 hPa. Both fields exhibit a westward tilt with height, with positive boundary layer specific specific humidity anomalies extending more than 120° ahead of the reference longitude, but mid-tropospheric anomalies are more confined to the convective center of the MJO. RH anomalies have a similar westward tilt throughout the depth of the troposphere, but then take on an opposite, eastward tilt with height near the tropopause, similar to the structure found for the MJO-related RH in Adames and Wallace (2015). The zonal circulation has a double overturning cell pattern, and produces a single large subsidence region away from the convective center of the MJO. In this way the zonal overturning circulation provides greater context for the equatorial zonal wind anomalies observed in Fig. 8a-b.

Moving to the Q50 case in Fig. 9b, we see that the magnitude of the RH anomalies at the center of the MJO have increased considerably. Along with this increase in magnitude, the westward tilts of the moisture fields have been reduced; lower-tropospheric specific humidity anomalies are now confined primarily to within 60° of the reference longitude, and upper-tropospheric RH anomalies lie roughly over top of the lower-tropospheric anomalies. The overturning circulation has seemingly become more complex. There is now a region of subsidence around 60° ahead of the reference longitude, associated with the leading overturning cell of the MJO that is now separate from the subsidence of the lagging overturning cell. This appears to assist in shallowing the positive specific humidity anomalies leading the region of deep convection.

In the Q100 case (Fig. 9c), the magnitude of the RH anomalies has now decreased relative to the Q50 case. The positive specific humidity anomalies have been further confined to the convective center of the MJO. The main subsidence region is now associated with the lagging overturning cell of the zonal circulation, however this regions has shifted further westward such that it resides closer to the leading edge of the MJO. This results in strong negative specific humidity anomalies in the lower troposphere between 60°-180° ahead of the reference longitude.

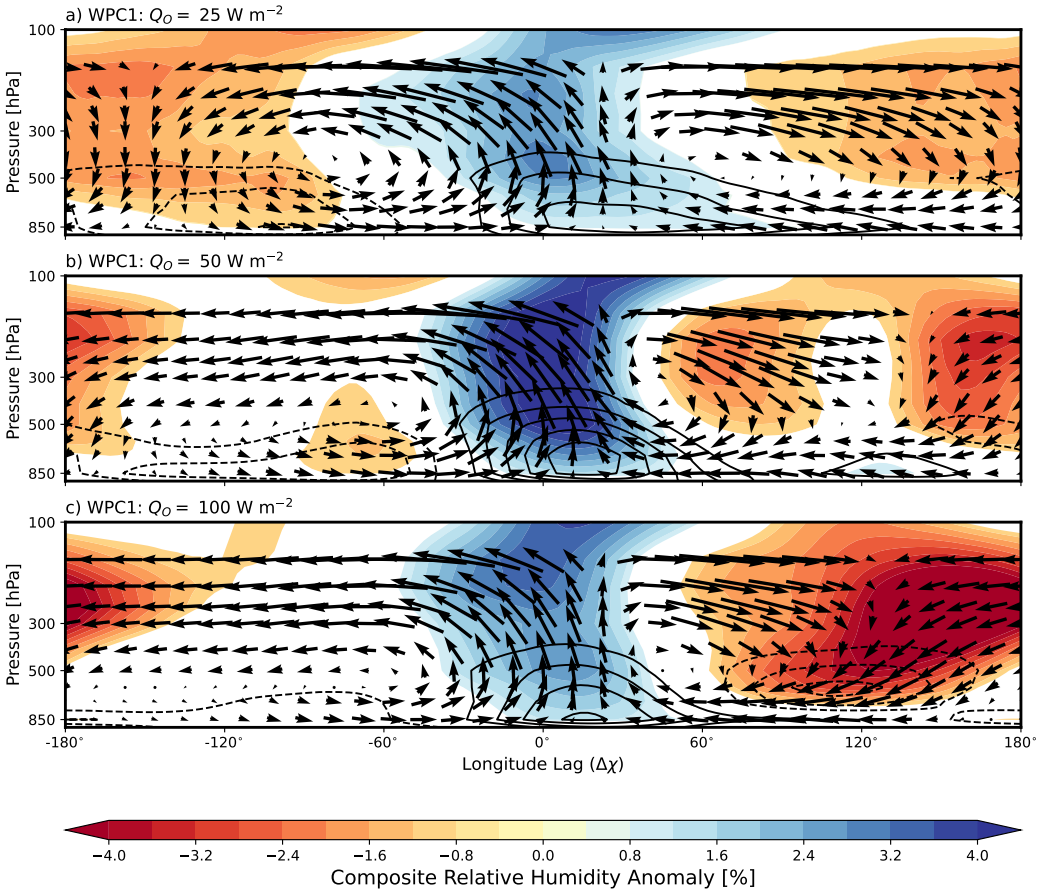

FIG. 9. WPC1 of RH (shading), specific humidity (contours), and equatorial overturning circulation ((u,ω) vectors) anomalies for (a) the Q25 run, (b) the Q50 run and (c) the Q100 run. The contour interval for the specific humidity is 0.04 g kg^{-1}, and the zero contour is omitted. The ω values for the vectors have been scaled by -10^2 to improve visualization and have upward arrows correspond to ascending motion. Values which do not pass the statistical significance test are masked with white.

d. Vertical Structures of the Vertical Velocity

Reanalysis studies of the MJO suggest that the vertical structure of the vertical velocity is dominated by a first baroclinic mode, with ascent throughout the depth of the troposphere that maximizes at a mid-tropospheric level around 400 hPa (Adames and Wallace 2014b, 2015). The residual structure of the vertical velocity largely takes on a second baroclinic mode with opposing motion in the lower- and upper- troposphere, corresponding to either shallow or stratiform convection. Shallow convection is observed leading the center of the MJO and stratiform convection

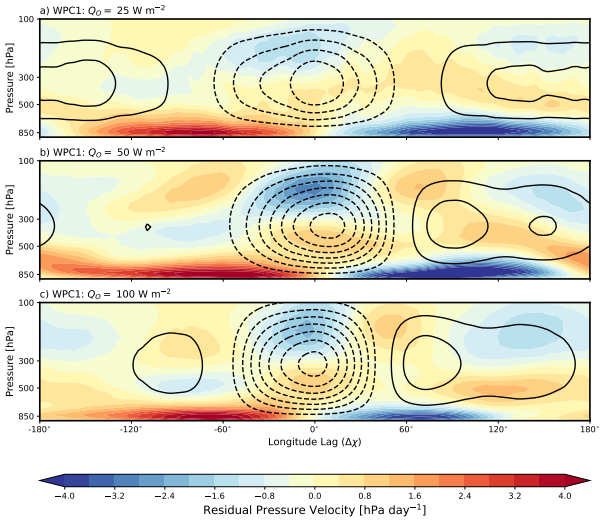

FIG. 10. Equatorial plane of WPC1 for the first baroclinic mode of the intraseasonally-filtered vertical velocity (black contours) and the residual structure (shading) for (a) the Q25 experiment, (b) the Q50 experiment and (c) the Q100 experiment. The contour interval is 2 hPa day^{-1}, with negative values dashed and the zero contour omitted.

trailing it, lending the divergence field of the MJO its characteristic westward tilt with height (Adames and Wallace 2014b; Zhang et al. 2020). To evaluate the importance of these different vertical structures to the destabilization and propagation of the MJO mode, we use the PCA method described in Adames and Wallace (2014b) to decompose the three-dimensional regression map of the MJO vertical velocity field into a series of vertical modes and horizontal maps as

$$\omega(x,y,p) = \sum_{k=1}^{N_\ell} \omega_k(x,y)\Lambda_\omega^{(k)}(p), \tag{7}$$

where ω_k are a set of horizontal maps which describe the modal structure of the vertical velocity, $\Lambda_\omega^{(k)}$ are their corresponding vertical structures and N_ℓ is the number of vertical levels. $\Lambda_\omega^{(1)}$ then corresponds to the deep convective mode, $\Lambda_\omega^{(2)}$ the shallow or stratiform mode depending on the sign of the horizontal map, and more complex vertical structures will be represented by the remaining terms of the expansion.

The contours in Fig. 10 show WPC1 of the first baroclinic mode of the vertical velocity filtered to intraseasonal time scales for the Q25, Q50 and Q100 experiments. For the Q25 experiment (Fig. 10a) the ascent region occupies about 120° of longitude, with maximum ascent occurring directly

over the reference longitude at around 400 hPa. The anomalous subsidence region occupies the rest of the equatorial plane, with maximum descent trailing the convective center of the MJO mode. For the Q50 experiment (Fig. 10b), the ascent region of the MJO has been confined to a smaller sector of the equator, but has a stronger maximum ascent. The maximum in subsidence now occurs immediately ahead of the region of deep convection. Intraseasonal first baroclinic vertical velocities for the Q100 case (Fig. 10c) greatly resemble those of the Q50 case.

The residual WPC1 structures (the full intraseasonal vertical velocity minus the contribution of the first baroclinic mode) for each experiment are shown as the shading in Fig. 10. For all three experiments, the residual structure is dominated by a region of shallow convection ahead of the reference longitude and stratiform convection trailing. In the Q25 experiment, this region of shallow convection extends more than 180° ahead of the reference longitude. For the Q50 experiment, the shallow convection has been confined to a smaller extent ahead of the MJO center, but has increased in magnitude. Additionally, the region of upper-tropospheric subsidence above the shallow convection has increased in strength. More complex structures of vertical velocity start to become more prominent away from the reference longitude. The Q100 experiment exhibits a similar structure, but the shallow convection has weakened significantly and does not penetrate as far into the lower-troposphere, nor as far ahead of the reference longitude.

4. Sensitivity of the MJO to Model Parameters

a. Sensitivity to Mixed Layer Depth

We now investigate the sensitivity of the MJO produced by our model to a few important parameters. The first parameter we vary is the depth of the ocean mixed layer by performing experiments in the Q50 configuration with the depth of the mixed layer increased to 20 m and 100 m. Fig. 11 shows the resulting space-time spectra of the signal strength of equatorial precipitation for these runs, with Fig. 11a corresponding to the previously presented Q50 case. The spectra for the runs with mixed layer depths of 20 m and 100 m are shown in Fig. 11b and Fig. 11c, respectively. The two deeper mixed layer cases look very similar in all spectral regions. In particular, there is more significant high frequency Kelvin wave activity when deeper mixed layers are used, and weakened MJO-like variability, though there is still significant signal along the 6 m s^{-1} phase speed line at intraseasonal time scales. It should also be noted that in a zonally symmetric

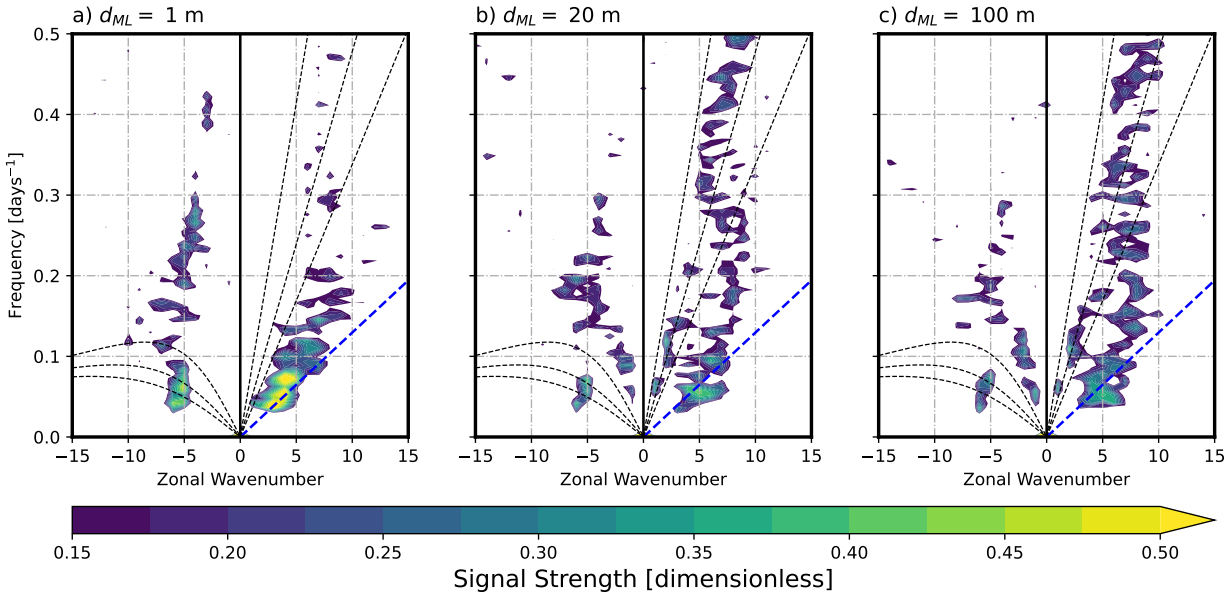

595 FIG. 11. As in Fig. 5 but for the Q50 configuration with mixed layer depths of (a) 1 m (the previously shown
596 Q50 run), (b) 20 m and (c) 100 m.

607 state, deeper mixed layers are less favorable to producing MJO-like variability; whereas the control
608 run with a mixed layer depth of 1 m still produced some weak signal in the MJO spectral region
609 (Fig. 5a), a mixed layer depth of 20 m produces no significant MJO-like variability and instead
610 supports planetary scale Kelvin waves (not shown).

611 Altering the ML depth of the model also has an impact on the the spatial distribution of
612 precipitation within the simulated MJO. With a deeper slab the longitudinal position of the off-
613 equatorial precipitation anomalies, which for both the observed MJO and our simulations with
614 a ML depth of 1 m (Fig. 7b) lie to the west of the convective center of the MJO, are shifted
615 significantly eastward. This shift lends a horizontal structure to the MJO which is mirrored relative
616 to its usual distribution; the usual swallow-tail shape of the MJO points in the opposite direction
617 (not shown).

618 *b. Sensitivity to Convection Scheme Parameters*

619 We next vary the two parameters which control the behavior of the model's convection scheme.
620 We use two additional runs of the model in the Q50 configuration with the RH_{SBM} parameter
621 decreased to 60% and increased to 80% from its control value of 70%. Space-time spectra of

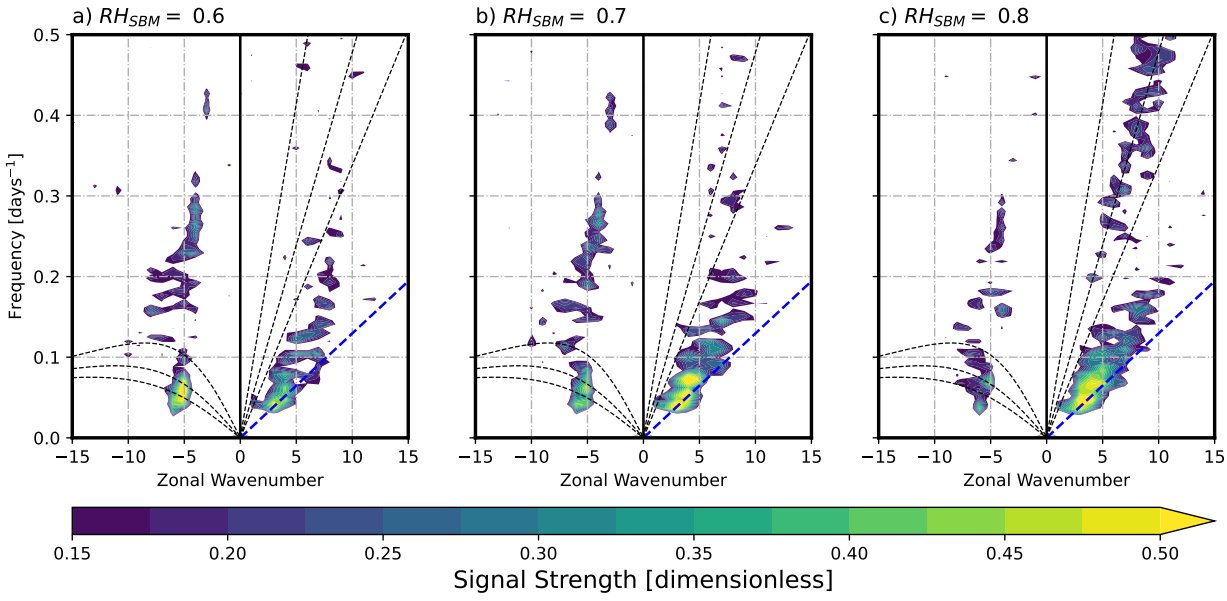

FIG. 12. As in Fig. 5 but for experiments with RH_{SBM} set to (a) 60%, (b) 70% (the previously shown Q50 run), and (c) 80%.

equatorial precipitation for these runs are shown in Fig. 12, with Fig. 12b corresponding to the unperturbed Q50 experiment. When RH_{SBM} is made smaller (Fig. 12a), the main impact is seen at intraseasonal time scales, both as an increase in the signal strength from equatorial Rossby waves and as a decrease in the signal strength of the MJO. Conversely, upon increasing RH_{SBM} to 80%, a reduction in Rossby wave signal and increase in MJO signal is observed. Alongside these changes at intraseasonal time scales, increasing RH_{SBM} also enhances the variability of higher frequency Kelvin waves at times scales between 2 and 10 days. Frierson (2007a) observed a similar enhancement of convectively-coupled equatorial Kelvin wave activity upon increasing RH_{SBM} over a similar range, before seeing a reduction is spectral power when using values close to saturation (RH_{SBM} = 0.95).

We also run one further experiment with the moist convective adjustment time τ_{SBM} increased to 16 h in the Q50 configuration. This has the effect of weakening the strength of the intraseasonal variability, though the MJO still remains by far the strongest mode of tropical variability. The spurious high frequency Kelvin wave signal that was present in the unperturbed Q50 experiment is now completely eliminated, consistent with the sensitivity experiments of Frierson (2007a), in which increasing τ_{SBM} to a value of 8 h removed virtually all Kelvin wave variability.

Fig. 13 shows a Hövmoller plot of equatorial precipitation for the run with the larger τ_{SBM}. While there are still eastward-propagating disturbances on the intraseasonal time scale, the nature of these disturbances has changed. Whereas the time series in Fig. 4 show their respective MJO events as coherent bands of precipitation propagating eastward across the warm pool, in Fig. 13 the events have more distinct pockets of precipitation that arise progressively eastward with time, while individual pockets move westward. This kind of convective organization is found in the observed MJO as well (Nakazawa 1988; Madden and Julian 1994). Frierson (2007b) found that running the gray-radiation equivalent of this model with τ_{SBM} = 16 h made tropical precipitation organize into much smaller pockets of intense precipitation dominated by large-scale condensation, in contrast to the more smeared out features observed when the SBM convection scheme was included. This change was accompanied by a transition to a stronger HC and stronger mean precipitation at the equator. Our simulations show a similar transition to a stronger HC and equatorial precipitation as τ_{SBM} is increased. However, the observed transition is weaker in our model than in Frierson (2007b); in their gray-radiation model the HC strength increased by 31% and equatorial precipitation increased by 57%, while for our model these quantities increase by 10% and 23%, respectively, in both the control and Q50 configurations. This suggests that the inclusion of interactive radiation in our model helps to stabilize the tropics and retain a weaker HC, and that this transition is relatively insensitive to the zonal asymmetry of the model.

These sensitivity experiments suggest that the coupling of the simulated MJO to moist convection is distinct from that of both equatorial Rossby waves and Kelvin waves. When the fraction of precipitation due to large-scale condensation is decreased (increased) by lowering (raising) $\mathrm{RH}_{\mathrm{SBM}}$, the model's convectively-coupled Rossby waves become stronger (weaker), yet the opposite effect is seen for the MJO mode. The behavior of the MJO mode also appears to be different from the Kelvin waves produced by the model; increasing τ_{SBM} drastically changes the way in which tropical convection aggregates and eliminates Kelvin wave variability, yet the tropics still support an MJO-like mode in this case.

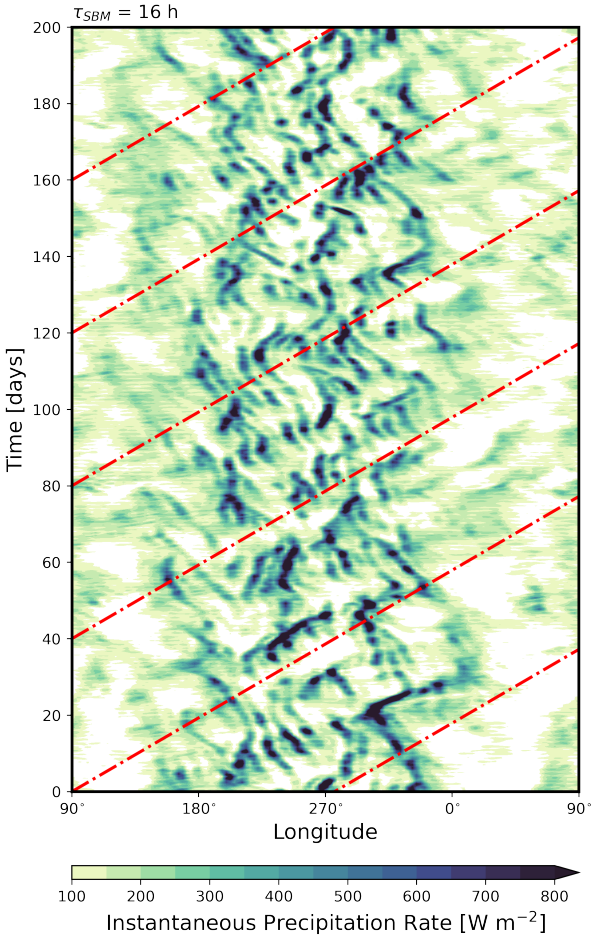

FIG. 13. As in Fig. 4 but for the Q50 experiment with the moist convective adjustment time τ_{SBM} increased to 16 h.

5. Column Moist Static Energy Budget

a. Column Moist Static Energy Budget in the GMS Plane

We now examine the column moist static energy (CMSE) budget of the MJO mode produced by our model. We focus here on the Q25 experiment, in which the three-dimensional structure of the simulated MJO mode resembles that of the observed MJO to a reasonable degree. Results for the Q50 and Q100 experiments are qualitatively similar. Analysis of the CMSE budget has been used extensively in past studies of the MJO to identify physical processes that contribute to its destabilization and propagation (Kiranmayi and Maloney 2011; Andersen and Kuang 2012;

Arnold et al. 2013; Carlson and Caballero 2016; Yasunaga et al. 2019). The Eulerian budgets for column dry static energy (CDSE) and column water vapor (CWV) are given by (Yanai et al. 1973)

$$\frac{\partial \langle s \rangle'}{\partial t} = -\nabla \cdot \langle s\mathbf{v} \rangle' + L_v P' + \langle Q_r \rangle' + H', \quad \text{and} \tag{8a}$$

$$\frac{\partial \langle L_v q \rangle'}{\partial t} = -\nabla \cdot \langle L_v q\mathbf{v} \rangle' - L_v P' + L_v E', \tag{8b}$$

where s is the dry static energy (DSE), q is the specific humidity, and $\mathbf{v}$ is the horizontal wind. The remaining terms represent the various diabatic forcings, where P is the precipitation rate, E is the surface evaporation rate, Q_r is the profile of radiative heating, H' is the sensible heat flux at the surface and L_v is the latent heat of vaporisation. Angle brackets denote pressure integrals from the surface to 100 hPa, where the pressure velocity ω is assumed to be zero, and primes denote quantities that have been spectrally filtered to intraseasonal (10-100 day) time scales and regressed onto an MJO index to produce an MJO-related anomaly, similar to the procedure outlined in Adames (2017). In both Eqs. 8a and Eq. 8b, the primary balance is between vertical advection of DSE or CWV and precipitation, with the time tendencies being relatively small residuals. By combining these two equations into a single equation for the MSE $h = s + L_v q$, we cancel these opposing contributions from precipitation and get an equation for the CMSE:

$$\frac{\partial \langle h \rangle'}{\partial t} = -\nabla \cdot \langle h\mathbf{v} \rangle' + \langle Q_r \rangle' + S', \tag{9}$$

where $S' = L_v E' + H'$ is the total surface flux of MSE. Following the derivation of Inoue and Back (2015b, 2017), Eq. 9 is then normalized by the anomalous column export of DSE $\nabla \cdot \langle s\mathbf{v} \rangle'$, which acts as a measure of the intensity of convection associated with the MJO. The CMSE budget can then be written in the form

$$\frac{1}{\nabla \cdot \langle s\mathbf{v} \rangle'} \frac{\partial \langle h \rangle'}{\partial t} = -(\Gamma' - \Gamma'_c), \tag{10}$$

where Γ' is the normalized anomalous gross moist stability (GMS) and Γ'_c is termed the normalized anomalous critical GMS. Since in this study we are concerned only with anomalous budgets of CMSE associated with the MJO, for simplicity we will refer to these quantities as the GMS and critical GMS, respectively. These are given by

$$\Gamma' = \frac{\nabla \cdot \langle h\mathbf{v} \rangle'}{\nabla \cdot \langle s\mathbf{v} \rangle'} \quad \text{and} \quad \Gamma'_c = \frac{\langle Q_r \rangle' + S'}{\nabla \cdot \langle s\mathbf{v} \rangle'}. \tag{11}$$

We can further decompose the GMS into its separate contributions from the horizontal and vertical advection of MSE by defining the horizontal and vertical GMS as

$$\Gamma'_h = \frac{\langle \mathbf{v} \cdot \nabla h \rangle'}{\nabla \cdot \langle s\mathbf{v} \rangle'} \quad \text{and} \quad \Gamma'_v = \frac{\langle \omega \partial h / \partial p \rangle'}{\nabla \cdot \langle s\mathbf{v} \rangle'}. \tag{12}$$

In a similar manner, the horizontal GMS can be further decomposed into its contributions from zonal and meridional advection Γ'_x and Γ'_y, and the critical GMS can be decomposed into contributions from radiative heating $\Gamma'_r = \langle Q_r \rangle' / \nabla \cdot \langle s\mathbf{v} \rangle'$ and surface fluxes $\Gamma'_s = S' / \nabla \cdot \langle s\mathbf{v} \rangle'$. The difference between the GMS and critical GMS $\Gamma' - \Gamma'_c$ is termed the drying efficiency. As in Inoue and Back (2015b, 2017), two different phases of the convective lifecycle can be identified based on the sign of the drying efficiency: an amplifying phase when the drying efficiency is negative and a decaying phase when the drying efficiency is positive. Inoue and Back (2017) showed that the GMS is a highly time-dependent quantity, but within that that time-dependence is a coherent cycle in the so-called "GMS-plane" of column divergence of DSE and MSE. A characteristic value of the GMS over the entirety of this cycle can then be determined via linear regression of the points in this plane, and the cycling behavior may be summarized by considering the GMS as a complex-valued parameter. It is this characteristic value (the real part of the GMS) which is relevant for many previous linear theories of the MJO (Inoue and Back 2017).

We employ the concept of the GMS-plane to look at the time-dependent behavior of the CMSE budget. The MJO-filtered time series of $\partial \langle h \rangle' / \partial t$, $\nabla \cdot \langle h\mathbf{v} \rangle'$ and $\langle Q_r \rangle' + S'$ are plotted against the column export of DSE $\nabla \cdot \langle s\mathbf{v} \rangle'$ for all equatorial points from the center of the warm pool (5°S-5°, 210°E-330°E). Following Inoue and Back (2017), the characteristic GMS value is calculated as

$$\Gamma_r = \frac{\{(\nabla \cdot \langle h\mathbf{v} \rangle')(\nabla \cdot \langle s\mathbf{v} \rangle')\}}{\{(\nabla \cdot \langle s\mathbf{v} \rangle')(\nabla \cdot \langle s\mathbf{v} \rangle')\}}, \tag{13}$$

where the curly brackets indicate an average across all times and spatial points. The imaginary part of the GMS, which measures the degree to which the GMS fluctuates around its characteristic value is given by

$$\Gamma_i = -\lambda_c \frac{\{(\nabla \cdot \langle h\mathbf{v} \rangle')(\partial \nabla \cdot \langle s\mathbf{v} \rangle'/\partial t)\}}{\{(\partial \nabla \cdot \langle s\mathbf{v} \rangle'/\partial t)(\partial \nabla \cdot \langle s\mathbf{v} \rangle'/\partial t)\}}, \tag{14}$$

where λ_c is a characteristic frequency for the MJO. For the MJO mode simulated by our model, we take this frequency to be $2\pi/(30 \text{ days})$. Definitions for the characteristic and fluctuating values of the critical GMS and drying efficiency are defined in a similar manner.

Fig. 14 shows the resulting orbits in the GMS-plane for the MJO-filtered (10-100 day period, zonal wavenumbers 1-10) time series of the CMSE budget terms using data from the center of the warm pool (5°S - 5°N, 210°E - 330°E) in the Q25 experiment. The scatterplot of column export of MSE versus column export of DSE in shown in Fig. 14a. Linear regression through the origin gives a positive characteristic GMS (note that in the figure the column export of MSE has been multiplied by -1), so that at the time of maximum convection, the combination of horizontal and vertical advection is removing MSE from the column. Fig. 14d shows the same scatterplot, but with colors indicating the fraction of points in which the strength of convection is increasing (i.e. $\partial \nabla \cdot \langle s\mathbf{v} \rangle'/\partial t > 0$). Here we can see that the times at which convection is increasing are associated with negative GMS, so that the combination of horizontal and vertical advection is acting to import MSE into the column. At times when convection is weakening, the GMS is higher than its characteristic value, and advection acts to damp CMSE anomalies. When the column export of MSE is decomposed into its contributions from horizontal and vertical advection, it is found the cycling behavior of the GMS is driven by horizontal advection, while the value of the characteristic GMS is determined primarily by vertical advection (not shown). Inoue and Back (2015a) found similar contributions from vertical and horizontal advection at intraseasonal time scales.

Figs. 14b and 14d show the combined contribution to the CMSE tendency from radiative heating and surface MSE fluxes. These two separate terms contribute roughly equal parts to the characteristic value of Γ_c'. The radiative heating component is strongly coupled to the strength of convection, and does not fluctuate around its characteristic value (not shown). The strength of the radiatve heating is also weak compared to its observed effect on Earth: anomalous radiative heating associated with the MJO is observed to be roughly linearly related to anomalous precipitation as

$$\langle Q_r \rangle' = r L_v P', \tag{15}$$

where r is a cloud-radiative feedback parameter (Kim et al. 2015; Adames and Kim 2016) which generally takes on a value of $r \approx 0.17$, though Adames and Kim (2016) suggested that this parameter may have some scale-dependence, so that planetary scale motions feel a stronger feedback than those at smaller scales. Parameters of this kind have seen extensive use in theoretical models of the MJO (Fuchs and Raymond 2002; Sobel and Maloney 2012; Adames and Kim 2016; Fuchs and Raymond 2017). Under the WTG approximation of Sobel et al. (2001), in which the time tendency of CDSE is ignored, and neglecting sensible heat fluxes Eq. 8a simplifies to a balance of the form

$$0 = -\nabla \cdot \langle s\mathbf{v} \rangle' + \langle Q_r \rangle' + L_v P'. \tag{16}$$

As shown in Inoue and Back (2015b), the radiative heating GMS can be related to the cloud-radiative feedback parameter as

$$r = \frac{\Gamma_r'}{1 - \Gamma_r'}. \tag{17}$$

In our model, where $\Gamma_r' \approx 0.03$, we will have $\Gamma_r' \approx r$. Thus the value of r in our model is about an order of magnitude smaller than observed for Earth. This is not entirely surprising; since our model has no clouds it relies only on radiation-water vapor interactions to produce this effect. However, cloud-radiative effects have been posited to play an important role in the destabilization of the MJO by reducing the "effective" GMS (Sobel and Maloney 2012; Adames and Kim 2016; Adames et al. 2019) that the MJO feels. It is interesting that our model is able to produce an MJO-like intraseasonal mode with this effect severely diminished.

The surface MSE flux on the other hand provides resistance to the propagation of the MJO by orbiting around its characteristic value in an opposite sense to GMS. Surface fluxes of sensible heat are small in the tropics (Inoue and Back 2017), so this term is dominated by the contribution from surface latent heat flux. This is consistent with the results of Adames (2017), who found that MJO-related surface evaporation anomalies played an analogous role in opposing the propagation of MJO precipitation, which should be approximately co-located with CMSE anomalies close to the equator.

Figs. 14c and 14f show the convective lifecycle of the time-tendency of CMSE. Like the GMS, the drying efficiency exhibits a wide orbit, which allows disturbances to continue to grow into the

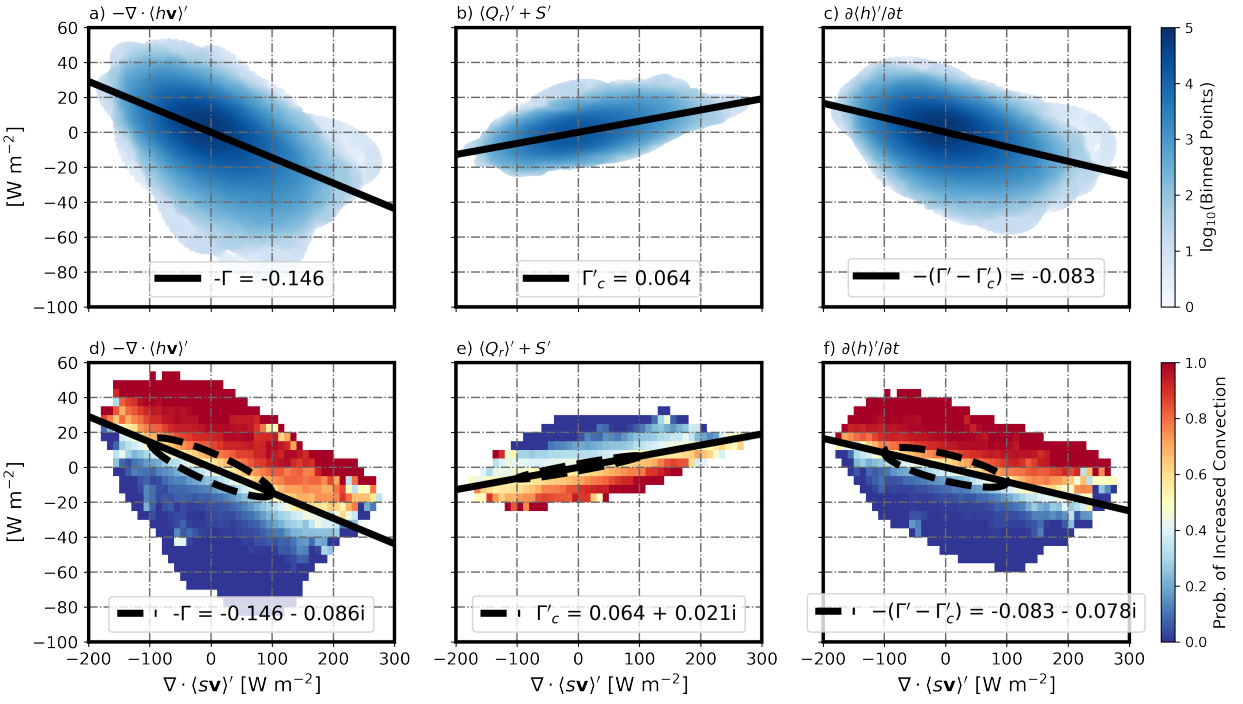

FIG. 14. Convective lifecycle of the CMSE budget using data from the center of the warm pool (5°S - 5°N, 210°E - 330°E) in the Q25 experiment. (a) scatterplot of $-\nabla\cdot\langle h\mathbf{v}\rangle'$ versus $\nabla\cdot\langle s\mathbf{v}\rangle'$, darker colors indicate a denser collection of scatter points, and the solid black line shows a regression through the origin. (b) as in panel (a) but for the diabatic source $\langle Q_r\rangle' + S'$ versus $\nabla\cdot\langle s\mathbf{v}\rangle'$. (c) as in panel (a) but for the CMSE time tendency $\partial\langle h\rangle'/\partial t$ versus $\nabla\cdot\langle s\mathbf{v}\rangle'$. (d) scatterplot of $-\nabla\cdot\langle h\mathbf{v}\rangle'$ versus $\nabla\cdot\langle s\mathbf{v}\rangle'$, gridded and colored by the fraction of points in each grid box in which the convection intensifies, the dashed black line shows the linearly regressed orbit in the GMS phase plane for convection with an amplitude of 100 W m^{-2}. (e) as in panel (d) but for $\langle Q_r\rangle' + S'$. (f) as in panel (d) but for $\partial\langle h\rangle'/\partial t$.

convectively active phase despite the characteristic value of drying efficiency being positive. The cycles of the individual budget terms should sum to this cycle. In reality, there will be a residual contribution due in part to the fact that the radiative heating rate, which is a model diagnostic, is integrated to the top of the atmosphere, while the advection terms of our budget are integrated to the assumed rigid lid at 100 hPa. The residuals are however small compared to the magnitude of the drying efficiency, suggesting that the budget is still approximately closed.

As previously discussed, Inoue and Back (2015b) showed that when a region is convectively active ($\nabla\cdot\langle s\mathbf{v}\rangle' > 0$), the sign of the drying efficiency identifies two different phases of the MJO: a

TABLE 1. Summary of GMS parameters calculated for the each individual term of the MJO-filtered CMSE budget for the Q25, Q50, and Q100 experiments.

Parameter	Definition	Q25	Q50	Q100
Γ'_x	$\langle u\partial h/\partial x\rangle'/(\nabla\cdot\langle s\mathbf{v}\rangle')$	-0.02 + 0.01i	0.01 + 0.02i	0.03 + 0.03i
Γ'_y	$\langle v\partial h/\partial y\rangle'/(\nabla\cdot\langle s\mathbf{v}\rangle')$	-0.05 + 0.06i	-0.05 + 0.05i	-0.08 + 0.04i
Γ'_v	$\langle \omega\partial h/\partial p\rangle'/(\nabla\cdot\langle s\mathbf{v}\rangle')$	0.22 + 0.02i	0.21 + 0.01i	0.20 + 0.01i
Γ'_r	$\langle Q_r\rangle'/(\nabla\cdot\langle s\mathbf{v}\rangle')$	0.03 + 0.00i	0.03 + 0.00i	0.03 + 0.00i
Γ'_s	$S'/(\nabla\cdot\langle s\mathbf{v}\rangle')$	0.04 + 0.02i	0.05 + 0.02i	0.04 + 0.02i
$\Gamma'-\Gamma'_c$	$-\partial\langle h\rangle'/\partial t/(\nabla\cdot\langle s\mathbf{v}\rangle')$	0.08 + 0.08i	0.10 + 0.08i	0.10 + 0.07i

negative drying efficiency corresponds to the amplification of convection while a positive drying efficiency corresponds to the decay of convection. The CMSE budget can then be viewed as a function of the drying efficiency itself, to see how the behavior of the budget changes as the convective lifecycle evolves. Figure 15 shows this evolution of the GMS and critical GMS as functions of the drying efficiency using the GMS plane orbits found in Fig. 14. When viewed in this way, the trajectories of the GMS parameters are linear functions of the drying efficiency. Binning the MJO-filtered time series of Γ' and Γ'_c by their drying efficiency produces similar linear trajectories (not shown). During the amplifying phase, the GMS (the red line) destabilizes the MJO mode, then switches sign and becomes a stabilizing influence during the decaying phase. The critical GMS (the blue line), which is dominated by the contribution from surface fluxes, provides opposition to the propagation of the MJO, indicated by the negative slope as a function of the drying efficiency. Thus the critical GMS acts opposite to the GMS, stabilizing the MJO during its amplifying phase and destabilizing it during the decaying phase of convection. A small residual (the grey line) exists since the drying efficiency is calculated from the time tendency of CMSE, while the GMS and critical GMS are calculated using advective and flux terms, respectively.

b. Connection to Linear Theories of the MJO

If we consider the MJO in a linear wave framework as a single, equatorially-trapped Fourier mode with wavenumber k and complex frequency λ, then the GMS quantities that were calculated in Section 5a become parameters of the linear model. In such a framework, the vertical velocity field may be assumed to be truncated to a single vertical mode that corresponds to deep convection

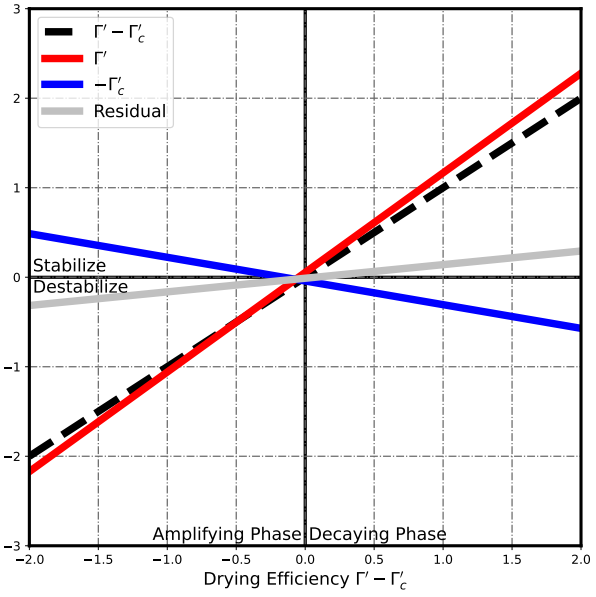

FIG. 15. Normalized CMSE budget of the simulated MJO budget in the Q25 experiment as a function of the drying efficiency. The GMS plane orbits of the GMS Γ' (red line), critical GMS Γ'_c (blue line) and drying efficiency $(\Gamma' - \Gamma'_c)$ (black dashed line) from Fig. 14 are plotted as functions of the drying efficiency itself. The residual of the CMSE budget is shown as a grey line.

throughout the depth of the troposphere (Fuchs and Raymond 2017; Adames et al. 2019). The anomalous vertical velocity related to the MJO can then be written as

$$\omega' = \omega_1 D_\omega(y)\Lambda_\omega(p) = \hat{\omega}_1 D_\omega(y)\Lambda_\omega(p)e^{i(kx-\lambda t)}, \tag{18}$$

where $\hat{\omega}_1$ is the amplitude of the vertical velocity, $D_\omega(y)$ its meridional structure, and $\Lambda_\omega(p)$ its vertical structure. The column export of DSE (which was used previously to measure the strength of convection) is tightly coupled to the first baroclinic vertical velocity, so that the gross dry stability M_s can be introduced to satisfy $-\nabla \cdot \langle s\mathbf{v}\rangle' = M_s\omega_1$. A value for M_s is determined in a similar manner to how the GMS parameters of Section 5a were calculated, with M_s assumed to be real-valued. The CMSE budget given in Eq. 9 may then be written as

$$-i\lambda\langle h\rangle' = \Gamma^*(\lambda, k)M_s\omega_1, \tag{19}$$

where $\Gamma^*(\lambda, k)$ is some general phase relation which depends on the specific physical parameterizations introduced by a linear model. For example, surface MSE fluxes and zonal MSE advection could be parameterized using the wind-induced surface heat exchange (WISHE) mechanism (Neelin et al. 1987; Emanuel 1987) which introduces a dependence on the zonal scale of the wave and prefers instability at planetary scales (Fuchs and Raymond 2005, 2017). Similarly radiative heating could be related to the precipitation rate through the cloud-radiative feedback parameter (Adames and Kim 2016; Adames et al. 2019), which can then be related back to the vertical velocity field through the CDSE equation. Here the focus will be on the simplest treatment possible for the CMSE equation, where Eq. 19 can be written in terms of the drying efficiency as

$$-i\lambda\langle h\rangle' = (\Gamma - \Gamma_c) M_s \omega_1, \tag{20}$$

where the drying efficiency $\Gamma - \Gamma_c$ is a complex parameter which does not depend on λ or k. It should be noted that this formulation implicitly includes contributions from higher order vertical modes; the contribution to the drying efficiency from vertical advection is calculated using the full vertical velocity field, rather than only the first baroclinic mode, so that the recharging of CMSE by shallow convection ahead of the MJO deep convection is still included. For simplicity, we will consider the case of no meridional flow ($v = 0$). Such frameworks have been used in the past to gain insight into the MJO and other equatorially trapped waves (Fuchs and Raymond 2017; Adames et al. 2019; Ahmed 2021). With no meridional flow, the meridional momentum equation reduces to a Sverdrup balance which gives the meridional structure that is common to all fields in the model. This simplification alleviates the need to solve an eigenvalue problem for multiple meridional structures. Furthermore, with this assumption only eastward-propagating modes may exist, as westward modes ($k < 0$) will not decay away from the equator. In this setting, the Appendix shows that the CDSE may be approximated as $\langle s\rangle' \approx iM_s\lambda\omega_1/(c^2k^2)$, where c is the phase speed of dry gravity waves and is given by $c = (R_d M_s/(C_p\langle\Lambda_T\rangle))^{1/2}$, where R_d is the specific gas constant for air, C_p the specific heat capacity and $\langle\Lambda_T\rangle$ the pressure integral of the vertical structure of the temperature field. In this way we get a dry gravity wave speed of $c \approx 51$ m s^{-1}, close to observed values for Earth (Kiladis et al. 2009). The governing equations for the system are then given by

$$\frac{M_s}{c^2}\frac{\lambda^2}{k^2}\omega_1 = M_s\omega_1 + L_v P', \quad \text{and} \tag{21a}$$

$$-i\lambda\langle h\rangle' = (\Gamma - \Gamma_c) M_s \omega_1, \tag{21b}$$

where the contributions to the CDSE tendency from radiative heating and surface sensible heat fluxes have been neglected as being small relative to the diabatic forcing provided by the precipitation term.

To close the system of equations, a parameterization of the precipitation term is required. This is done via a Betts-Miller type closure of the form

$$L_v P' = \frac{L_v}{\tau_c}\langle q\rangle' = \frac{1}{\tau_c}\left(\langle h\rangle' - i\frac{M_s}{c^2}\frac{\lambda}{k^2}\omega_1\right), \tag{22}$$

where τ_c is a moist convective relaxation timescale. Such closures have been used extensively in previous linear theories of the MJO and other equatorial disturbances (Sobel and Maloney 2012; Adames and Kim 2016; Fuchs and Raymond 2017; Adames et al. 2019). Figure 16a shows a representation of τ_c in the phase plane of MJO-related precipitation and CWV. τ_c exhibits a small orbit around its characteristic value, but is still tightly coupled to the precipitation. Thayer-Calder and Randall (2009) also found cyclical paths in the MJO precipitation-CWV phase plane using both model and observational data. We find that $\tau_c \approx 9.5 - 1.8i$ hr, shorter than the values used in Adames and Kim (2016) and Adames et al. (2019), but still notably distinct from the model's convective adjustment time, $\tau_{\text{SBM}} = 2$ hr.

With this parameterization in hand, the anomalous CMSE $\langle h\rangle'$ may be eliminated between Eq. 21a and 21b to get the the following dispersion relation:

$$\tau_c\lambda^3 + i\lambda^2 - c^2k^2\tau_c\lambda - ic^2k^2(\Gamma - \Gamma_c) = 0. \tag{23}$$

As in Fuchs and Raymond (2017) and Adames et al. (2019), this relation yields two damped modes and a single undamped mode at planetary scales. The solid blue lines in Fig. 16b and 16c show the frequency and growth rate of this unstable mode, respectively. As in Fuchs and Raymond (2017), this $v = 0$ mode has a faster phase speed than the observed MJO (shown by the black dash-dotted line in Fig. 16b). The mode also exhibits a westward group velocity for $k > 2$. The growth rate of the mode remains positive for a range of k that extends just slightly past $k = 1$, and has a magnitude that is weaker than the solutions of Fuchs and Raymond (2017) and Adames et al. (2019).

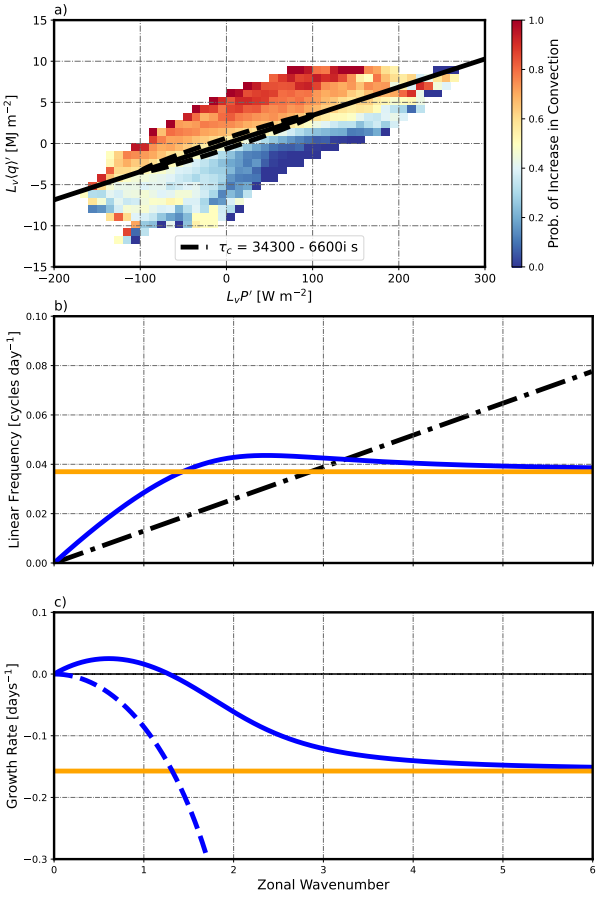

Fig. 16. (a) Representation of τ_c in the phase plane of MJO precipitation and CWV. (b) Linear frequency $\mathrm{Re}(\lambda)/(2\pi)$ for the undamped mode of the full dispersion relation (blue line) and the simplified WTG solution (orange line). The black dash-dotted line shows the 6 m s^{-1} phase speed line. (c) Growth rate for the undamped mode of the full dispersion relation (blue line) and the WTG solution (orange line). The dashed blue line shows the solution of the full dispersion relation when the imaginary part of the drying efficiency is neglected.

This dispersion relation may be simplified by neglecting the 2nd and 3rd order terms in λ. Physically, this is equivalent to invoking the assumptions of WTG balance: the time tendency of the CDSE is assumed to be small, and the time tendency of the CMSE is then assumed to be dominated by its contribution from the moisture tendency. Eq. 21a and 21b may then be written as

$$0 = M_s\omega_1 + L_vP' \quad \text{and} \tag{24a}$$

$$-i\lambda\left(\langle h\rangle' - i\frac{M_s}{c^2}\frac{\lambda^2}{k^2}\omega_1\right) = (\Gamma - \Gamma_c)M_s\omega_1. \tag{24b}$$

Solving this system for λ then yields the simplified dispersion relation

$$\lambda = -\frac{i}{\tau_c}(\Gamma - \Gamma_c). \tag{25}$$

It is clear from Eq. 25 that in this WTG setting, the real part of the drying efficiency determines whether the mode will be unstable, and the imaginary part determines the speed at which the wave propagates. The solid orange lines in Fig. 16b and 16c show the linear frequency and growth rate of this mode. Both the frequency and the growth rate of the mode are insensitive to the zonal scale of the wave, meaning the mode's phase speed scales with $1/k$ and it is damped equally at all zonal wavenumbers. This suggests that due to the weak radiative heating associated with the MJO in our model, the modes cannot be destabilized in a WTG setting. This is in contrast to the $v = 0$ WTG mode discussed in Adames et al. (2019), where strong cloud-radiation interactions adequately lowered the effective GMS to make the mode unstable at planetary scales. Fuchs and Raymond (2017) also found that their WISHE moisture mode was damped in a WTG setting in the absence of cloud-radiative feedbacks.

The dashed blue line in Fig. 16c shows the growth rate of the mode when the imaginary parts of $\Gamma - \Gamma_c$ and τ_c are neglected. Making this alteration eliminates the instability at planetary scales. This suggests that the convective lifecycle of vertical advection and other CMSE budget terms, which is encapsulated by allowing the GMS parameters and hence the drying efficiency to be complex-valued, is essential to the existence of an instability at planetary scales in the absence of WISHE or cloud-radiative feedbacks.

6. Discussion

Many previous attempts have been made to produce MJO-like disturbances in idealized settings [see Jiang et al. (2020) for a comprehensive review of modelling efforts related to the MJO]. Here we will discuss how our study relates to a few of these attempts. While in our model the application of a zonally asymmetric forcing was required to make the MJO-like disturbances the dominant mode of tropical intraseasonal variability, many other studies have been successful in generating an MJO mode in a variety of zonally symmetric aquaplanet configurations. Andersen and Kuang (2012) used the Super-Parameterized Community Atmosphere Model (SP-CAM) to generate MJO-like disturbances, and Arnold et al. (2013) found that MJO variability was enhanced

at higher sea-surface temperature (SST) in the same model. Carlson and Caballero (2016) used the Community Atmosphere Model (CAM) with a conventional convection scheme coupled to a slab ocean with prescribed ocean heat transports to show that the MJO was enhanced after multiple doublings of the atmospheric carbon dioxide mixing ratio, and was accompanied by a transition to a superrotating state. Khairoutdinov and Emanuel (2018) used a cloud-resolving model (CRM) in a channel setup about the equator to generate a MJO-like mode. In their respective analyses of the intraseasonal CMSE budget, all of these studies identify long-wave radiative heating as playing the most important role in destabilizing the MJO. However, the mechanism denial experiments of Arnold and Randall (2015) suggested that SP-CAM still has some ability to produce an MJO without cloud-radiation feedbacks. Our model also suggests that intraseasonal modes can be generated without strong radiation feedbacks, as the lack of clouds makes radiative heating a much smaller contributor to the CMSE budget. The necessary condition of zonal asymmetry to produce an appreciable MJO in our model suggests that stronger convection-radiation feedbacks are a necessary condition for the MJO instability to grow from small perturbations in a zonally symmetric model. Many of these symmetric models also produce very consistent and regular MJO events when equatorial OLR or precipitation are viewed in Hövmoller plots (Andersen and Kuang 2012; Arnold et al. 2013; Khairoutdinov and Emanuel 2018), whereas our model produces more variability in the time between initiation of MJO events.

Other studies have emphasized the importance of the warm pool to the generation of an appreciable MJO signal. Maloney et al. (2010) showed that their model, which produced a weak MJO in its zonally symmetric configuration, could produce a stronger MJO when the fixed SST distribution was modified to mimic the observed equatorial distribution of Earth. However, their model also required a weakening of the extratropical SST meridional gradient to get a strong MJO. Our model, which lacks ocean heat transport, has a strong gradient of surface temperature in the extratropics yet still produces an MJO-like mode, suggesting differences in the way idealized and comprehensive models respond to the introduction of a warm pool. The earlier work of Bladé and Hartmann (1993) also emphasized the importance of zonal asymmetry in a two-layer model with a conditional instability of the second kind (CISK) model of convective heating. The presence of a zonal temperature gradient highlighted fundamental differences between moist Kelvin waves which circumnavigated the equatorial band and the "CISK-modes" which were unique to

the warm pool sector. This led them to attribute the intraseasonal time scale of their CISK-mode to localized convective processes in the warm pool, rather than the global propagation of the Kelvin modes. Simple, local models of convection have also suggested an intrinsic intraseasonal time scale for convective processes (Hu and Randall 1994; Sobel and Gildor 2003). Bladé and Hartmann (1993) associated this timescale with the rapid increase of static stability during the time of active convection (discharge) and the slow reduction of static stability during convectively inactive times (recharge). Our model undergoes a similar transition in atmospheric stability, here measured using the GMS, with negative GMS prior to the time of maximum convection and positive GMS afterwards. That the two most important parameters in our linear model, the drying efficiency and moist convective adjustment time, essentially describe the behavior of local convective processes suggests further synergy with the recharge-discharge picture of intraseasonal oscillations.

Bladé and Hartmann (1993) also used this setup to show the importance of extratropical influences on the initiation of the MJO. New disturbances appeared as stationary signals of upper-level divergence formed from the intrusion of mid-latitude eddies into the tropics before beginning to propagate eastward. They further argued that the stochastic nature of this forcing meant that it would not be seen in analysis of composite disturbances. Some of the MJO events in our model also begin as stationary convective regions (Fig. 4c). More recent work (Ray et al. 2009; Ray and Zhang 2010) have emphasized the key role that extratropical influences play in the initation of individual MJO events. Future work with our model should investigate the role that extratropical eddies play in MJO onset both for individual disturbances and in a composite sense, particularly in the context of the various tropical mean states that can be generated by varying the strength of the asymmetric forcing. It would be interesting to see what role the development of the KR pattern of stationary eddy divergence with stronger zonal temperature gradients may play in initiating MJO events.

Another striking feature of our model is its response to changes in the ML depth of the bottom boundary. It was found that the strength of MJO events increased monotonically as the ML depth was decreased. This is in contrast to the results of Maloney and Sobel (2004), where it was found that intraseasonal precipitation was maximized at a moderate ML depth of 20 m relative to both shallower and deeper depths. A similar nonmonotonic response to changes in ML depth was seen in the zero-dimensional model of Sobel and Gildor (2003) when forced at intraseasonal

time scales. In the models of both Sobel and Gildor (2003) and Maloney and Sobel (2004), the strength of surface radiative fluxes into the slab ocean were linked to cloud-radiation feedbacks by assuming that clouds modulate downward shortwave radiative fluxes with the same strength that they reduce the long-wave radiative cooling to space. In our model the net surface shortwave flux at the equator is reduced when precipitation is largest, but the strength of this effect is reduced relative to the assumption of Sobel and Gildor (2003), just as the convection-radiation feedback is relatively weak. Thus the different dependency of our model upon the ML depth may also be linked to the simple treatment of moist convection.

7. Conclusions

In this study we have shown that MJO-like variability may be induced in an idealized moist GCM by introducing zonal asymmetry through a wavenumber-1 ocean heat flux. The simulated MJO was able to reproduce many of the characteristics of the observed MJO: slow (6 m s^{-1}) propagation eastward across the warm pool sector, swallow-tail spatial structure of precipitation and westward tilt with height were all reproduced by the model. Extratropical Rossby waves associated with the MJO, both on the equatorward flank of the STJ and in the mid-latitudes were also generated by our model. The strength of this MJO mode appeared to be strongest when the surface temperature difference between the warm pool and cold pool was around 5 K (the Q50 experiment). Further increasing the asymmetry produced a peculiar bistable regime, where high frequency Kelvin waves and the MJO mode dominated tropical variability at different times. The application of this asymmetric forcing also had profound effects on the mean state of the simulations; a transition to superrotation in the tropical upper-troposphere and a weakening of the Hadley cell were observed as the contrast between the cold pool and warm pool was increased. This was accompanied by a moistening of the subtropics of the cold hemisphere, so that thermodynamic fields take on a KR pattern. However, the meridional flux of MSE was insensitive to the imposition of zonal asymmetry.

The MJO mode generated in our model was sensitive to the ML depth of the underlying slab ocean. The strongest MJO variability was seen at very shallow ML depths, though the mode was still present when the ML depth was deeper. The behavior of the MJO mode was also sensitive to the configuration of the model's convection scheme. Upon increasing (decreasing) the relative

humidity of the reference moisture profile the MJO mode became stronger (weaker). Interestingly, the MJO-like variability is retained when the moist convective adjustment time of the convection scheme was increased by a factor of 8; this alteration drastically changed the way equatorial precipitation organized, yet precipitation anomalies were still seen to propagate slowly across the warm pool sector. It is one of the strengths of our study that there are only two parameters to adjust in the SBM convection scheme; studies using more comprehensive GCMs (e.g. Hannah and Maloney 2014; Klingaman and Woolnough 2014a,b) have shown a strong dependence on the parameters of more complicated convection schemes.

An analysis of the CMSE budget of the MJO modes revealed that advection of MSE plays a dominant role in setting the so-called "drying efficiency" of the atmosphere. Prior to the arrival of the MJO, advection acts to charge the column with MSE before transitioning to removing MSE from the column when convection is at a maximum. The combinations of surface fluxes and radiative heating act opposite to advection, stabilizing the MJO while convection intensifies and destabilizing it while convection diminishes. Since there are no clouds in the model, the contribution of radiative heating to the maintenance of the MJO mode is severely diminished relative to its effect on the observed MJO. It is the generation of an MJO-like disturbance without an appreciable contribution from cloud-radiative feedbacks which is perhaps the most interesting result of this study. It suggests an expanded role for the hierarchy of atmospheric models in understanding the physical mechanisms of the MJO.

A linear stability analysis in the simplified $\nu = 0$ case using parameters derived from our model suggested that instability may be produced at planetary scales without appealing to either WISHE or cloud-radiative feedbacks to act as a destabilizing influence. In particular, modelling the convective lifecycle of the MJO mode by allowing the drying efficiency and moist convective adjustment time to be complex-valued parameters was found to be essential to producing a planetary-scale instability. Enforcing WTG balance lead to the mode being damped equally at all length scales, as the convection-radiation feedbacks were too weak to sufficiently reduce the effective GMS as is required in other moisture mode theories (Adames et al. 2019). Future work will look at more comprehensive ($\nu \neq 0$) linear theories which can produce moisture modes which bear greater qualitative resemblance to the observed MJO to see what role the convective lifecycle viewpoint can play in destabilizing these models.

The initiation of MJO events in our model was not explored in this study, but should be considered as a vital topic for future investigations. In particular, the role of the extratropics in exciting MJO events on the western flank of the warm pool has been discussed in previous work (Bladé and Hartmann 1993; Ray et al. 2009; Ray and Zhang 2010). In the context of our model, we also believe it would be fruitful to explore how changes to the atmosphere's mean state with increased asymmetric forcing may affect the ability of extratropical disturbances to initiate MJO events.

Acknowledgments. The authors acknowledge GFDL resources made avaialbe for this research. The authors thank Spencer Clark for assistance in configuring and running the numerical model used in this study. Comments from Isaac Held and Ángel Adames-Corraliza greatly improved the quality of the manuscript.

Data availability statement. The numerical experiments performed in this study were carried out using the National Oceanic and Atmospheric Administration (NOAA) Geophysical Fluid Dynamics Laboratory's (GFDL) Flexible Modeling System (FMS). FMS can be accessed at https://www.gfdl.noaa.gov/fms/.

APPENDIX

Phase Relation between CDSE and First Baroclinic Pressure Velocity

The linearized, $v = 0$ momentum, continuity, and hydrostatic equations truncated to a first baroclinic mode on the equatorial β-plane are given by (e.g. Fuchs and Raymond 2017; Adames et al. 2019)

$$\frac{\partial u'}{\partial t} = -\frac{\partial \phi'}{\partial x}, \tag{A1a}$$

$$\beta y u' = -\frac{\partial \phi'}{\partial y}, \tag{A1b}$$

$$\frac{\partial u'}{\partial x} = -\frac{\partial \omega'}{\partial p}, \quad \text{and} \tag{A1c}$$

$$\frac{\partial \phi'}{\partial \ln p} = -R_d T', \tag{A1d}$$

where u' is the zonal velocity anomaly, ϕ' is the geopotential anomaly, T' is the temperature anomaly and β is the meridional gradient of the planetary vorticity. We first note that eliminating u' between Eqs. A1a and A1b provides the meridional structure $D(y)$ that is common to all the fields, which must satisfy

$$\frac{\mathrm{d}D(y)}{\mathrm{d}y} = -\frac{\beta k}{\lambda} y D(y). \tag{A2}$$

This equation can be solved to yield a meridional strucutre given by

$$D(y) = \exp(-\frac{\beta k}{2\lambda} y^2), \tag{A3}$$

which limits our solutions to only eastward propagating modes, as westward modes ($k < 0$) will not decay away from the equator. Eqs. A1 also stipulate certain relations between the vertical structures of the various fields. The conditions provided by the zonal momentum, continuity, and hydrostatic equations are respectively given by

$$\Lambda_u(p) = \Lambda_\phi(p), \tag{A4a}$$

$$\Lambda_u(p) = -\frac{\mathrm{d}\Lambda_\omega(p)}{\mathrm{d}p}, \quad \text{and} \tag{A4b}$$

$$\frac{\mathrm{d}\Lambda_\phi(p)}{\mathrm{d}\ln p} = \Lambda_T(p). \tag{A4c}$$

Removing the common vertical and meridional dependence, Eqs. A1a, A1c and A1d may be expressed as

$$\lambda u_1 = k\phi_1, \tag{A5a}$$

$$iku_1 = \omega_1, \quad \text{and} \tag{A5b}$$

$$\phi_1 = -R_d T_1. \tag{A5c}$$

The anomalous DSE is given by $s' = C_p T' + \phi'$, so that the vertically integrated anomalous DSE may be written as

$$\langle s \rangle' = R_d T_1 (C_p \langle \Lambda_T \rangle / R_d - \langle \Lambda_\phi \rangle), \tag{A6}$$

where Eq. A5c has been used to relate the geopotential anomaly to the temperature anomaly. The term in the brackets is dominated by its first term, related to the vertical integral of temperature, so the contribution from $\langle \Lambda_\phi \rangle$ is neglected. Eqs. A5 may then be used to relate the vertically integrated DSE anomaly to the pressure velocity as

$$\langle s \rangle' = i \frac{C_p}{R_d} \frac{\lambda}{k^2} \langle \Lambda_T \rangle \omega_1. \tag{A7}$$

The square of the dry gravity wave speed can then be defined as $c^2 = R_d M_s/(C_p\langle\Lambda_T\rangle)$ so that the anomalous CDSE may be written as

$$\langle s\rangle' = i\frac{M_s}{c^2}\frac{\lambda}{k^2}\omega_1. \tag{A8}$$

References

Adames, Á. F., 2017: Precipitation budget of the madden–julian oscillation. *Journal of the Atmospheric Sciences*, **74 (6)**, 1799–1817.

Adames, Á. F., and D. Kim, 2016: The mjo as a dispersive, convectively coupled moisture wave: Theory and observations. *Journal of the Atmospheric Sciences*, **73 (3)**, 913–941.

Adames, Á. F., D. Kim, S. K. Clark, Y. Ming, and K. Inoue, 2019: Scale analysis of moist thermodynamics in a simple model and the relationship between moisture modes and gravity waves. *Journal of the Atmospheric Sciences*, **76 (12)**, 3863–3881.

Adames, Á. F., and E. D. Maloney, 2021: Moisture mode theory's contribution to advances in our understanding of the madden-julian oscillation and other tropical disturbances. *Current Climate Change Reports*, **7 (2)**, 72–85.

Adames, Á. F., and J. M. Wallace, 2014a: Three-dimensional structure and evolution of the mjo and its relation to the mean flow. *Journal of the Atmospheric Sciences*, **71 (6)**, 2007–2026.

Adames, Á. F., and J. M. Wallace, 2014b: Three-dimensional structure and evolution of the vertical velocity and divergence fields in the mjo. *Journal of the Atmospheric Sciences*, **71 (12)**, 4661–4681.

Adames, Á. F., and J. M. Wallace, 2015: Three-dimensional structure and evolution of the moisture field in the mjo. *Journal of the Atmospheric Sciences*, **72 (10)**, 3733–3754.

Ahmed, F., 2021: The mjo on the equatorial beta plane: An eastward-propagating rossby wave induced by meridional moisture advection. *Journal of the Atmospheric Sciences*, **78 (10)**, 3115–3135.

Andersen, J. A., and Z. Kuang, 2012: Moist static energy budget of mjo-like disturbances in the atmosphere of a zonally symmetric aquaplanet. *Journal of Climate*, **25 (8)**, 2782–2804.

Arnold, N. P., Z. Kuang, and E. Tziperman, 2013: Enhanced mjo-like variability at high sst. *Journal of Climate*, **26 (3)**, 988–1001.

Arnold, N. P., and D. A. Randall, 2015: Global-scale convective aggregation: Implications for the madden-julian oscillation. *Journal of Advances in Modeling Earth Systems*, **7 (4)**, 1499–1518.

Benedict, J. J., and D. A. Randall, 2007: Observed characteristics of the mjo relative to maximum rainfall. *Journal of the atmospheric sciences*, **64 (7)**, 2332–2354.

Betts, A., and M. Miller, 1986: A new convective adjustment scheme. part ii: Single column tests using gate wave, bomex, atex and arctic air-mass data sets. *Quarterly Journal of the Royal Meteorological Society*, **112 (473)**, 693–709.

Bladé, I., and D. L. Hartmann, 1993: Tropical intraseasonal oscillations in a simple nonlinear model. *Journal of Atmospheric Sciences*, **50 (17)**, 2922–2939.

Bretherton, C. S., M. E. Peters, and L. E. Back, 2004: Relationships between water vapor path and precipitation over the tropical oceans. *Journal of climate*, **17 (7)**, 1517–1528.

Carlson, H., and R. Caballero, 2016: Enhanced mjo and transition to superrotation in warm climates. *Journal of Advances in Modeling Earth Systems*, **8 (1)**, 304–318.

Chen, G., and B. Wang, 2018: Does the mjo have a westward group velocity? *Journal of Climate*, **31 (6)**, 2435–2443.

Clark, S. K., Y. Ming, and Á. F. Adames, 2020: Monsoon low pressure system–like variability in an idealized moist model. *Journal of Climate*, **33 (6)**, 2051–2074.

Clark, S. K., Y. Ming, I. M. Held, and P. J. Phillipps, 2018: The role of the water vapor feedback in the itcz response to hemispherically asymmetric forcings. *Journal of Climate*, **31 (9)**, 3659–3678.

Emanuel, K. A., 1987: An air-sea interaction model of intraseasonal oscillations in the tropics. *Journal of Atmospheric Sciences*, **44 (16)**, 2324–2340.

Frierson, D. M., 2007a: Convectively coupled kelvin waves in an idealized moist general circulation model. *Journal of the atmospheric sciences*, **64 (6)**, 2076–2090.

Frierson, D. M., 2007b: The dynamics of idealized convection schemes and their effect on the zonally averaged tropical circulation. *Journal of the atmospheric sciences*, **64 (6)**, 1959–1976.

Frierson, D. M., I. M. Held, and P. Zurita-Gotor, 2006: A gray-radiation aquaplanet moist gcm. part i: Static stability and eddy scale. *Journal of the atmospheric sciences*, **63 (10)**, 2548–2566.

Frierson, D. M., I. M. Held, and P. Zurita-Gotor, 2007: A gray-radiation aquaplanet moist gcm. part ii: Energy transports in altered climates. *Journal of the Atmospheric Sciences*, **64 (5)**, 1680–1693.

Fuchs, Ž., and D. J. Raymond, 2002: Large-scale modes of a nonrotating atmosphere with water vapor and cloud–radiation feedbacks. *Journal of the atmospheric sciences*, **59 (10)**, 1669–1679.

Fuchs, Z., and D. J. Raymond, 2005: Large-scale modes in a rotating atmosphere with radiative–convective instability and wishe. *Journal of the atmospheric sciences*, **62 (11)**, 4084–4094.

Fuchs, Ž., and D. J. Raymond, 2017: A simple model of intraseasonal oscillations. *Journal of Advances in Modeling Earth Systems*, **9 (2)**, 1195–1211.

Gill, A. E., 1980: Some simple solutions for heat-induced tropical circulation. *Quarterly Journal of the Royal Meteorological Society*, **106 (449)**, 447–462.

Hannah, W. M., and E. D. Maloney, 2014: The moist static energy budget in ncar cam5 hindcasts during dynamo. *Journal of Advances in Modeling Earth Systems*, **6 (2)**, 420–440.

Hu, Q., and D. A. Randall, 1994: Low-frequency oscillations in radiative-convective systems. *Journal of Atmospheric Sciences*, **51 (8)**, 1089–1099.

Inoue, K., and L. Back, 2015a: Column-integrated moist static energy budget analysis on various time scales during toga coare. *Journal of the Atmospheric Sciences*, **72 (5)**, 1856–1871.

Inoue, K., and L. E. Back, 2015b: Gross moist stability assessment during toga coare: Various interpretations of gross moist stability. *Journal of the Atmospheric Sciences*, **72 (11)**, 4148–4166.

Inoue, K., and L. E. Back, 2017: Gross moist stability analysis: Assessment of satellite-based products in the gms plane. *Journal of the Atmospheric Sciences*, **74 (6)**, 1819–1837.

Jiang, X., and Coauthors, 2020: Fifty years of research on the madden-julian oscillation: Recent progress, challenges, and perspectives. *Journal of Geophysical Research: Atmospheres*, **125 (17)**, e2019JD030 911.

Khairoutdinov, M. F., and K. Emanuel, 2018: Intraseasonal variability in a cloud-permitting near-global equatorial aquaplanet model. *Journal of the Atmospheric Sciences*, **75 (12)**, 4337–4355.

Kiladis, G. N., M. C. Wheeler, P. T. Haertel, K. H. Straub, and P. E. Roundy, 2009: Convectively coupled equatorial waves. *Reviews of Geophysics*, **47 (2)**.

Kim, D., M.-S. Ahn, I.-S. Kang, and A. D. Del Genio, 2015: Role of longwave cloud–radiation feedback in the simulation of the madden–julian oscillation. *Journal of Climate*, **28 (17)**, 6979–6994.

Kiranmayi, L., and E. D. Maloney, 2011: Intraseasonal moist static energy budget in reanalysis data. *Journal of Geophysical Research: Atmospheres*, **116 (D21)**.

Klingaman, N., and S. Woolnough, 2014a: The role of air–sea coupling in the simulation of the madden–julian oscillation in the hadley centre model. *Quarterly Journal of the Royal Meteorological Society*, **140 (684)**, 2272–2286.

Klingaman, N., and S. Woolnough, 2014b: Using a case-study approach to improve the madden–julian oscillation in the hadley centre model. *Quarterly Journal of the Royal Meteorological Society*, **140 (685)**, 2491–2505.

Kraucunas, I., and D. L. Hartmann, 2005: Equatorial superrotation and the factors controlling the zonal-mean zonal winds in the tropical upper troposphere. *Journal of the atmospheric sciences*, **62 (2)**, 371–389.

Lutsko, N. J., 2018: The response of an idealized atmosphere to localized tropical heating: Superrotation and the breakdown of linear theory. *Journal of the Atmospheric Sciences*, **75 (1)**, 3–20.

Madden, R. A., and P. R. Julian, 1971: Detection of a 40–50 day oscillation in the zonal wind in the tropical pacific. *Journal of Atmospheric Sciences*, **28 (5)**, 702–708.

Madden, R. A., and P. R. Julian, 1972: Description of global-scale circulation cells in the tropics with a 40–50 day period. *Journal of Atmospheric Sciences*, **29 (6)**, 1109–1123.

Madden, R. A., and P. R. Julian, 1994: Observations of the 40–50-day tropical oscillation—a review. *Monthly weather review*, **122 (5)**, 814–837.

1175 Majda, A. J., and S. N. Stechmann, 2009: The skeleton of tropical intraseasonal oscillations.
1176 *Proceedings of the National Academy of Sciences*, **106 (21)**, 8417–8422.

1177 Majda, A. J., and S. N. Stechmann, 2011: Nonlinear dynamics and regional variations in the mjo
1178 skeleton. *Journal of the Atmospheric Sciences*, **68 (12)**, 3053–3071.

1179 Maloney, E. D., and D. L. Hartmann, 1998: Frictional moisture convergence in a composite life
1180 cycle of the madden–julian oscillation. *Journal of climate*, **11 (9)**, 2387–2403.

1181 Maloney, E. D., and A. H. Sobel, 2004: Surface fluxes and ocean coupling in the tropical intrasea-
1182 sonal oscillation. *Journal of Climate*, **17 (22)**, 4368–4386.

1183 Maloney, E. D., A. H. Sobel, and W. M. Hannah, 2010: Intraseasonal variability in an aquaplanet
1184 general circulation model. *Journal of Advances in Modeling Earth Systems*, **2 (2)**.

1185 Matsuno, T., 1966: Quasi-geostrophic motions in the equatorial area. *Journal of the Meteorological*
1186 *Society of Japan. Ser. II*, **44 (1)**, 25–43.

1187 Merlis, T. M., T. Schneider, S. Bordoni, and I. Eisenman, 2013: Hadley circulation response to
1188 orbital precession. part i: Aquaplanets. *Journal of Climate*, **26 (3)**, 740–753.

1189 Nakazawa, T., 1988: Tropical super clusters within intraseasonal variations over the western pacific.
1190 *Journal of the Meteorological Society of Japan. Ser. II*, **66 (6)**, 823–839.

1191 Neelin, J. D., I. M. Held, and K. H. Cook, 1987: Evaporation-wind feedback and low-frequency
1192 variability in the tropical atmosphere. *Journal of Atmospheric Sciences*, **44 (16)**, 2341–2348.

1193 O'Gorman, P. A., and T. Schneider, 2008: The hydrological cycle over a wide range of climates
1194 simulated with an idealized gcm. *Journal of Climate*, **21 (15)**, 3815–3832.

1195 Paynter, D., and V. Ramaswamy, 2014: Investigating the impact of the shortwave water vapor
1196 continuum upon climate simulations using gfdl global models. *Journal of Geophysical Research:*
1197 *Atmospheres*, **119 (18)**, 10–720.

1198 Ray, P., and C. Zhang, 2010: A case study of the mechanics of extratropical influence on the
1199 initiation of the madden–julian oscillation. *Journal of the atmospheric sciences*, **67 (2)**, 515–
1200 528.

Ray, P., C. Zhang, J. Dudhia, and S. S. Chen, 2009: A numerical case study on the initiation of the madden–julian oscillation. *Journal of the Atmospheric Sciences*, **66 (2)**, 310–331.

Raymond, D. J., S. L. Sessions, A. H. Sobel, and Ž. Fuchs, 2009: The mechanics of gross moist stability. *Journal of Advances in Modeling Earth Systems*, **1 (3)**.

Rostami, M., and V. Zeitlin, 2019: Eastward-moving convection-enhanced modons in shallow water in the equatorial tangent plane. *Physics of Fluids*, **31 (2)**, 021 701.

Saravanan, R., 1993: Equatorial superrotation and maintenance of the general circulation in two-level models. *Journal of Atmospheric Sciences*, **50 (9)**, 1211–1227.

Showman, A. P., and L. M. Polvani, 2011: Equatorial superrotation on tidally locked exoplanets. *The Astrophysical Journal*, **738 (1)**, 71.

Sobel, A., and E. Maloney, 2012: An idealized semi-empirical framework for modeling the madden–julian oscillation. *Journal of the Atmospheric Sciences*, **69 (5)**, 1691–1705.

Sobel, A., and E. Maloney, 2013: Moisture modes and the eastward propagation of the mjo. *Journal of the Atmospheric Sciences*, **70 (1)**, 187–192.

Sobel, A. H., and H. Gildor, 2003: A simple time-dependent model of sst hot spots. *Journal of Climate*, **16 (23)**, 3978–3992.

Sobel, A. H., J. Nilsson, and L. M. Polvani, 2001: The weak temperature gradient approximation and balanced tropical moisture waves. *Journal of the atmospheric sciences*, **58 (23)**, 3650–3665.

Suarez, M. J., and D. G. Duffy, 1992: Terrestrial superrotation: A bifurcation of the general circulation. *Journal of Atmospheric Sciences*, **49 (16)**, 1541–1554.

Thayer-Calder, K., and D. A. Randall, 2009: The role of convective moistening in the madden–julian oscillation. *Journal of the Atmospheric Sciences*, **66 (11)**, 3297–3312.

Wang, B., and H. Rui, 1990: Dynamics of the coupled moist kelvin–rossby wave on an equatorial b-plane. *J. Atmos. Sci*, **47 (4)**, 397–413.

Welch, P., 1967: The use of fast fourier transform for the estimation of power spectra: a method based on time averaging over short, modified periodograms. *IEEE Transactions on audio and electroacoustics*, **15 (2)**, 70–73.

Wheeler, M., and G. N. Kiladis, 1999: Convectively coupled equatorial waves: Analysis of clouds and temperature in the wavenumber–frequency domain. *Journal of the Atmospheric Sciences*, **56 (3)**, 374–399.

Wheeler, M. C., and H. H. Hendon, 2004: An all-season real-time multivariate mjo index: Development of an index for monitoring and prediction. *Monthly weather review*, **132 (8)**, 1917–1932.

Wolding, B. O., and E. D. Maloney, 2015: Objective diagnostics and the madden–julian oscillation. part ii: Application to moist static energy and moisture budgets. *Journal of Climate*, **28 (19)**, 7786–7808.

Yanai, M., S. Esbensen, and J.-H. Chu, 1973: Determination of bulk properties of tropical cloud clusters from large-scale heat and moisture budgets. *Journal of Atmospheric Sciences*, **30 (4)**, 611–627.

Yang, D., and A. P. Ingersoll, 2013: Triggered convection, gravity waves, and the mjo: A shallow-water model. *Journal of the atmospheric sciences*, **70 (8)**, 2476–2486.

Yang, D., and A. P. Ingersoll, 2014: A theory of the mjo horizontal scale. *Geophysical Research Letters*, **41 (3)**, 1059–1064.

Yano, J.-I., and J. J. Tribbia, 2017: Tropical atmospheric madden–julian oscillation: a strongly nonlinear free solitary rossby wave? *Journal of the Atmospheric Sciences*, **74 (10)**, 3473–3489.

Yasunaga, K., S. Yokoi, K. Inoue, and B. E. Mapes, 2019: Space–time spectral analysis of the moist static energy budget equation. *Journal of Climate*, **32 (2)**, 501–529.

Zhang, C., Á. Adames, B. Khouider, B. Wang, and D. Yang, 2020: Four theories of the madden-julian oscillation. *Reviews of Geophysics*, **58 (3)**, e2019RG000 685.